https://doi.org/10.15407/ufm.20.03.447

Yu.F. IVANOV[1,2], D.V. ZAGULYAEV[3], S.A. NEVSKII[3], V.E. GROMOV[3], V.D. SARYCHEV[3], and A.P. SEMIN[3]

[1] Institute of High-Current Electronics, SB RAS, 2/3 Akademicheskiy Ave., 634055 Tomsk, Russia

[2] National Research Tomsk Polytechnic University, 2/3 Akademicheskiy Ave., 634055 Tomsk, Russia

[3] Siberian State Industrial University, 42 Kirov Str., 654007 Novokuznetsk, Russia

MICROSTRUCTURE AND PROPERTIES OF HYPOEUTECTIC SILUMIN TREATED BY HIGH-CURRENT PULSED ELECTRON BEAMS

The structural-phase states, microhardness, and tribological properties of hypoeutectic silumin after electron-beam treatment are studied by the methods of contemporary physical materials science. The object of the study is hypoeutectic AK10M2H-type silumin containing 87.88 wt.% of Al and 11.1 wt.% of Si as the base components. The silumin surface is subjected to electron-beam treatment in six various regimes distinct in the density of electron-beam energy. The microhardness measurements of the modified silumin-surface layers enabled to determine three optimal impact regimes (with electron-beam energy densities of 25, 30, and 35 J/cm^2), when the modified-layer microhardness exceeds that for the cast silumin. The obtained parameters are as follow: 0.86 ± 0.41 GPa for the cast state; 0.93 ± 0.52 GPa for 25 J/cm^2; 0.97 ± 0.071 GPa for 30 J/cm^2; 0.96 ± 0.103 GPa for 35 J/cm^2. As found, the electron-beam treatment with the optimal parameters results in the formation of the surface whose mechanical and tribological characteristics sufficiently exceed corresponding values for the cast state of silumin. The atomic-force microscopy data correlate with the results on microhardness. The samples treated in the presented regimes are characterised with the fine-grained cellular structure and have the least roughness of the treated layer (of 17–33 nm) and substrate (of 45–57 nm) as compared to other regimes. As revealed, in the treated layer, the fine-grained, graded, and cellular structure is formed, and it transforms into the mixed-type structure when deepening away from the surface of treatment. Depending on the parameters of electron-beam treatment, the thickness of homogenized layer varies and reaches the maximum values of 100 μm at the energy density of 35 J/cm^2. As detected, the modified layer is free from intermetallides and consists of the nanocrystalline structure of cellular crystallization. As assumed,

these two factors are responsible for the increased mechanical and tribological characteristics of the modified layer. The formation mechanism for structure of cellular and columnar crystallization consisting in the initiation of thermocapillary instability over the 'evaporated substance/liquid phase' interface is offered. The mathematical model of the thermal effect of electron beam on the silumin-surface layers is developed.

Keywords: physical nature, mathematical model, structure, properties, hypoeutectic silumin, electron beam treatment, phase composition.

1. Introduction

One of the most promising methods of surface hardening of materials, demonstrating its high effectiveness, is electron-beam treatment [1–5]. It ensures the ultrahigh rates of heating (up to 10^6 K/s) of surface layer at a present temperature and the cooling of surface layer at the expense of heat removal in the bulk of the material at the rates of 10^4–10^9 K/s with the result formation of nonequilibrium submicro- and nanocrystalline structural-phase states [1].

The type of treatment being considered has wide possibilities of the supplied energy checking, the small coefficients of energy reflection, the high concentration of energy in the volume unite of the material [2]. The electron-beam treatment has a number of advantages over other methods of surface modification. In comparison with the powerful ion beams, the electron-beam treatment has a substantially higher efficiency in pulse-frequency regime at smaller accelerating voltages and needs no special radiation protection. The high-energy efficiency, the high homogeneity of energy density in the streamwise section, the good susceptibility of pulses, and their high pulse-repetition rate give a number of advantages over the pulsed flow of low temperature plasma [3–5].

The main advantage of the electron beam treatment (EBT) is the combination of actually complete absorption of electron energy with the possibility of variation of depth of electrons' penetration in the material and, respectively, the dynamics of thermal fields and the parameters of stress wave.

To estimate the modern state of the scientific problem, let us consider some papers, in which the problem of electron-beam effect on different materials as the method of their hardening was discussed.

The authors of the paper [6] investigated the mechanical properties of YG10X carbide irradiated by high-current pulsed electron beam with the constant energy density of 6 J/cm^2 and different number of pulses. Vickers hardness served as the described mechanical characteristic more completely reflecting the state of the material after the electron-beam radiation. For the untreated sample, the microhardness amounted to ≈2165 *HV* on the average in different regimes of loading. As established

in the course of the study, the irradiation by high-current pulsed electron beam resulted in 1.5–2-fold increase in microhardness of the material. The tribological studies showed that the friction coefficient after 10 pulses decreased 3-fold from the initial state. The improved tribological properties were connected, mainly, with the effect of hardening of composite microstructure. In Ref. [7], it was established that not only the increase in the number of pulses of treatment but also the change in the parameter of electron beam current could lead to the increase in microhardness. Microhardness of Ti–47Al–2Cr–2Nb (here and hereinafter, in wt.%) alloy increases with the increase in the beam current from 4.5 mA to 8.5 mA and amounts to 330.45 *HV* at beam current from 4.5 mA and 368.98 *HV* for the sample with beam current 8.5 mA, it is by 11.66% higher.

The studies of electron beam treatment are carried out using not only the volume materials but also various coatings. The electron-beam effect various energy at 20 pulses on the nanohardness and roughness of TiN coating [8] was studied. It was found that nanohardness decreased to ≈25 GPa at energy density of 3 J/cm^2, ≈24 GPa at density of irradiation energy of 5 J/cm^2, as compared to the initial value of ≈26 GPa. With the further increase in the density of irradiation energy to 8 J/cm^2, the nanohardness of the irradiated coating TiN decreases abruptly to ≈10 GPa. It is possible that it is connected with the appearance and distribution of the surface cracks on irradiation. On the contrary, the roughness of the coating increases with the density growth of electron beam energy. It is detected that interphase adhesion is essentially higher for the irradiated sample with 5 J/cm^2 than for the samples irradiated by energy of 3 J/cm^2 and 8 J/cm^2. Ti–5Al–4V alloy [9] may be used as the substrate being irradiated. TiN/TiO_2 coatings were applied to the substrate; then, the system was subjected to treatment by pulsed electron beam. It was found that electron-beam treatment resulted in the decrease in the microhardness value of the material with respect to the initial state from 7 to 6 GPa, the friction coefficient value decreased and, on the contrary, the roughness of the surface increased from 8 nm to 25 nm.

The latest researches carried out when using the samples of Al–15Si hypereutectic alloy showed that the treatment by high-current pulsed electron beam increased the tensile strength of the treated alloy by 41.4% from 138.8 MPa (for the initial sample) to 196.2 MPa for the modified sample. Thus, the treatment by high-current pulsed electron beam is the universal method for the improvement of the mechanical properties of hypereutectic alloys of Al–Si system [10].

The main scientific trend of the study of electron-beam treatment effect is the way of precision modification of structural-phase states and, therefore, the surface properties and surface layers of metallic materials.

By methods of scanning electron microscopy, the samples of Ti–36Nb–2Ta–3Zr–0.35O alloy [11] after the electron-beam treatment were studied. It is found that, in the initial state, the alloy has a sufficient quantity of pores, while the treated samples were characterized by low porosity. The x-ray diffraction patterns show that the samples treated by the intense electron beam have β-phase as the base one. The depth of melting of the surface layers of the material depends on the density of beam energy and rate of treatment. The effect of scanning rate by electron beam on the structure of Al–3Ti–1Sc alloys was described in Ref. [12]. It was detected that the rate of electron-beam treatment played the key role in the determination of phase composition and the development of microstructure in the alloy: the increase in the treatment rate and beam energy resulted in the increase in the area and depth of the surface remelting. As the substrate from Al–3Ti–1Sc was cast in the low-cooling conditions and Ti and Sc concentration increased substantially in the equilibrium solubility limit, a large number of the initial intermetallic phases were present in the microstructure; however, after the electron-beam treatment, the initial intermetallic phases were not observed. With the increase in the scanning rate, higher concentrations of Sc and Ti in the substrate than in the initial state were observed as well.

The performed studies on the high-current electron beam effect on the structure and properties of the commercial magnesium alloys of AZ91HP-type showed that the formation of the crater defects takes place on the irradiation, but with the increase in the number of treatment pulses, the tendency to the decrease in the defect and their disappearance [13] was observed. The formation mechanisms of defects under the effect of high-current pulsed electron beams were described in the earlier papers [14, 15]. The surface layer is melted to ≈8–10 μm depth where $Mg_{17}Al_{12}$ phase is practically absent under the effect of the pulsed treatment; the results of x-ray spectroscopic analysis support this phenomenon. It is also identified that, after electron-beam treatment, the diffraction peaks are displaced to the wide-angle side that can be indicative of the decrease in the lattice parameter of α(Mg)-phase with the increase in Al concentration.

In the review [16], the results of the experimental investigations into the EBT effect on the formation of properties, structure and phase composition of silumin surface layers are generalized.

Nowadays, the electron-beam effect on the materials is a complicated complex of the phenomena including the heating, melting, convective flows in the liquid layer, vaporization of substance, the consequent crystallization, and, as a result, the formation of the ordered structures of surface layers [17–22]. The columnar crystallization structure belongs to these structures. As the electron-microscopy investigations show [21, 22], the transverse dimension of these structures is of

≈0.1 nm–1 μm. The mechanism of their initiation on the surface of the melt can be connected with the development of thermocapillary instability [23] that is formed due to the action of thermocapillary forces along the surface of the melt. They arise because of the dependence of the surface tension on temperature and the presence of the stable gradient of temperature. Theoretical study of the instability of the molten layers of the materials under the action of laser radiation was performed in Refs. [24–30]. These papers show that the spectrum of surface perturbations of the molten layer of the viscous incompressible fluid at the initial stage of development is described by the algebraic dispersion equation connecting the frequency and module of wave vector. As a rule, the dispersion equation is lengthy, and it depends on many parameters; therefore, its numerical solution or finding of neutral curve is frequently used. It is the important information for the determination of the number of parameters at which the instability occurs. By means of the approach, the wave number is found, at which the rate of perturbation growth transits *via* naught, *i.e.* the critical wave number. It proved to be not enough because the wave numbers at which the maximum of growth rate arises play the important role. Therefore, the approximate formulae for obtaining of the dependence of the growth rate on the magnitude of wave number vector is necessary to be used for the obtaining of the physical consequences required for the analysis of conditions of the ordered structure formation of the surface layers. The approach based on the search for growth rate maximum was successfully used in Ref. [31] for the Kelvin–Helmholtz instability. In this paper, the dispersion equation that enables to perform the analytical parameterization and to obtain the important physical consequences [31], for example, the presence of two maximums, was derived for the short-wave approximation.

As follows from the papers discussed above, it was established that the application of electron beams for the treatment of metal surface resulted in change in structural-phase composition of surface layers and it, in its turn, led to the increase in the mechanical characteristics including wear resistance, microhardness and corrosion resistance as well.

In this connection, the goal of the study consists in the following. Firstly, the analysis of the experimental data of the change in the mechanical and tribological characteristics, structural-phase transformations in silumin under electron-beam treatment. Secondly, theoretical study of the mechanisms and the development of the mathematical model of the ordered structure formation in the surface layers of silumin under electron-beam treatment on the basis of the concepts of thermocapillary instability of the molten layers.

2. Object of the Study and Research Methods

The hypoeutectic alloy of silumin АК10М2Н (the grading refers to technical state standard GOST used in Russia) was used as test-material. The chemical composition of the material being tested was determined by the methods of x-ray spectrum analysis. As a result of the analysis, it was established that the base elements of its chemical composition are Al (87.88%) and Si (11.1%) diluted with balance admixtures of Cu, Ni, Mg, and Cr. The alloy of aluminium with silicon under consideration finds wide application in many branches of industry, in particular, in automobile construction in the manufacture of pistons of internal combustion engines.

The test samples had the dimensions of $20 \times 20 \times 10$ mm^3 and were oriented perpendicular to the electron beam. The surface modification was done using the plant 'SOLO' of the Institute of High Current Electronics at the SB RAS [32, 33].

The plant has the following main advantages over the earlier pulsed electron sources with plasma cathode: the high energy density in combination with a low accelerating voltage; the higher energy efficiency; the high range of parameter regulation; the good repeatability of pulses; the minimum time for preparation; the long service life [34].

The АК10М2Н silumin samples were irradiated by the intense pulsed electron beam in six regimes being distinguished by the energy density of electron beam (Table 1) and having the following identical parameters: the energy of accelerated electrons of 17 keV; the duration of electron beam pulse of 150 μs; the number of pulses — 3, the pulse repetition rate of 0.3 s^{-1}; the pressure of residual gas (argon) in the working chamber of $2 \cdot 10^{-2}$ Pa.

The metallographic analysis of structural changes was performed using optical microscope Olympus GX-51. For structural determination of the material by means of metallography, the samples were cut, ground, polished and etched. For the optical contrast, the samples were etched chemically by the solution containing 72% H_2O, 21% HF, and 7% HCl.

One of the most precision and sensitive methods — the measurement of microhardness — was used in the research as the characteristic of the mechanical properties of the surface layers. It is differences prior and after the treatment can serve as strain-hardening exponent of the modified surface layers of metals and alloys. The microhardness measu-

Table 1. **Regimes of silumin irradiation with high-intense electron beam**

No. of regime	*1*	*2*	*3*	*4*	*5*	*6*
Energy density E_s, J/cm^2	10	15	20	25	30	35

rements were done using the microhardness tester HVS-1000 by Vickers method [35]. The stable load for six regimes of treatment amounted to 0.05 N. The time of load application and load maintaining was of 10 s, and that of test load removal was of 5 s.

The tribological tests were performed according to the 'pin-on-disc' scheme at tribometer CSEM CH 2000 (at load P = 2 N and sliding velocity V = 10 mm/s; the counterbody diameter from ball bearing steel of 6 mm) in accordance with ASTM G99. The distance of friction was S = 20 m and radius of wear track r = 2 mm.

The investigation into the modified zone of silumin samples subjected to the electron-beam treatment were performed using atomic-force microscope NT-MDT Solver 'NEXT'. The samples had the dimensions of $5\times10\times10$ mm^3, and they passed the identical algorithm of preparation as those for microindentation and metallography.

The program Image Analysis 3.5 [36] was used for the processing of the obtained atomic-force images. By means of the program, the measurements of pores in the coating were made, the transition layer was studied and roughness of samples was determined as well.

The roughness estimation was done according to Russian Standard GOST 2789-73 using the function Standard statistics, where the standard statistical parameters characterizing the initial function $Z(x_j, y_j)$ (the recorded signal of feedback) as a random quantity Z [37] were represented. The main parameter for roughness estimate is the value Roughness average — the arithmetic mean value of roughness that reads as $R_a = (N_x N_y)^{-1} \sum_{j=1}^{N_y} \sum_{i=1}^{N_x} |Z_{ij}|$, where $N_x(N_y)$ is the quantity of points with $x(y)$ coordinates, and Z_{ij} is the value of Z coordinate.

The analysis of the elemental and phase compositions, defect structure of the modified layer was done by the methods of scanning electron microscopy (SEM) using the plants SEM-515 Philips equipped with microanalyzer EDAX ECON IV.

The determination of the chemical composition was performed by means of energy-dispersion detector of micro x-ray spectroscopic analysis INCAx-act. The elemental analysis of some phases was carried out by the method of electron-probe microanalysis that enabled to study the presence, content and distribution of the elements of Periodic Table.

The phase composition of the modified layers that is the qualitative and quantitative characteristics of the presence of different phases in them, their content, dispersion, structure and chemical composition were determined by the method of x-ray phase analysis (diffractometer XRD-7000 s, Shimadzu, Japan) in addition to the electron-diffraction microscopy.

The defect structure of the samples was analysed by the methods of transmission electron-diffraction microscopy of thin foils (plant JEM-

2100 F, JEOL) [38–40]. The images of fine structure of the material were used for the classification of the morphological indications of the structure [41].

The foils for the investigation into the structural phase state of the material by the methods of transmission electron-diffraction microscopy were prepared by ion thinning of ≈100 μm thick plates cut out the sample by the electrical spark method. The regime of cutting out was selected in such a way that it produced no additional deformation, and, consequently, it had no effects on the sample structure.

The plates cut out in such a way were thinned by ion etching method (plant Ion Slicer EM-09100 IS). The distinctive feature of the plant is that it requires no preparation of the disc thinned in the centre. The preliminary preparation of samples for Ion Slicer consists only in the manufacture of parallelepiped to the dimensions of $2.8 \times 0.5 \times 0.1$ mm that is closed from the thin wide end by the special protective tape and is thinned by the beam of argon ions. The beam energy is less than 8 kV, and the angle of incidence can be varied from 0° to 6° with respect to the largest face of the sample. It enables to minimize the radiation damages and, thereby, to conserve the initial structure and phase composition of the sample and, after it, to study them by the methods of electron microscopy.

3. Results and Discussions

3.1. Changes of Mechanical and Tribological Properties of Silumin after EBT

The dependence of change in microhardness of silumin surface on the energy density of electron beam is shown in Fig. 1. The increase of the energy density results in the monotonous increase in the microhardness value on the surface of irradiation. The maximum microhardness value is observed at energy density of electron beam of 30 J/cm^2. The further increase of the energy density up to 35 J/cm^2 results in the insignificant decrease of the microhardness value.

As the maximum values of surface microhardness are observed for values of 25, 30, and 35 J/cm^2, the studies of microhardness profile distribution depending on the distance to the surface of irradiation using the transverse metallographic sections were carried out. As the metal contains the grains of aluminium and eutectic, the microhardness measurements were carried out separately in the grain (Fig. 2, *c*) and in eutectic (Fig. 2, *b*).

It is determined that the microhardness values both in grains and in eutectic of the modified samples increase as the sprayed layer is approached (Fig. 3). It is discovered that irrespective of the treatment regimens the microhardness of samples in the zone subjected to irradia-

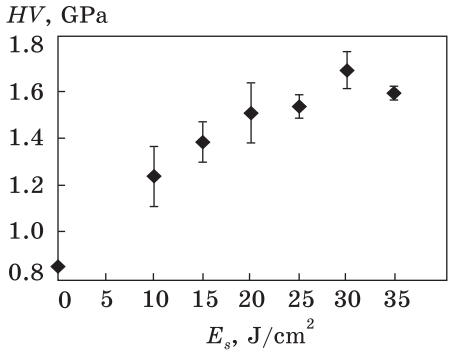

Fig. 1. Dependence of change of microhardness on energy density of electron beam

tion is larger than at 90 and 70 μm distances from the sample edge. The analysis of dependences gives grounds for making a conclusion that microhardness of silumin in eutectic is larger than in grains.

As seen in Fig. 3, *d*, microhardness value decreases as the bulk of the material is being approached and at 90 μm depth (0.93 ± 0.52 GPa for 25 J/cm^2; 0.97 ± 0.071 GPa for 30 J/cm^2; 0.96 ± 0.103 GPa for 35 J/cm^2) irrespective of the treatment regime.

According to the results of the investigation into the effect of electron-beam treatment on microhardness of silumin surface layers, the conclusion can be made that the optimal parameters of treatment which permit a 2-fold increase in microhardness are the regimes with energy density of 25, 30, 35 J/cm^2.

Having analysed the changes of microhardness of the samples being tested, the parameter of plasticity (Fig. 4) can be calculated.

As known, the characteristic of plasticity determined by the Vickers method can be defined in the form as follows [42]: $\delta = 1 - 1.1/(1 - \nu - 2\nu^2)$ HV/E, where HV is a microhardness magnitude, E is the Young modulus, ν is the Poisson's ratio of the material being studied.

The analysis of dependences of plasticity parameter δ on the distance to the surface of treatment shows that, in the zone of the modified

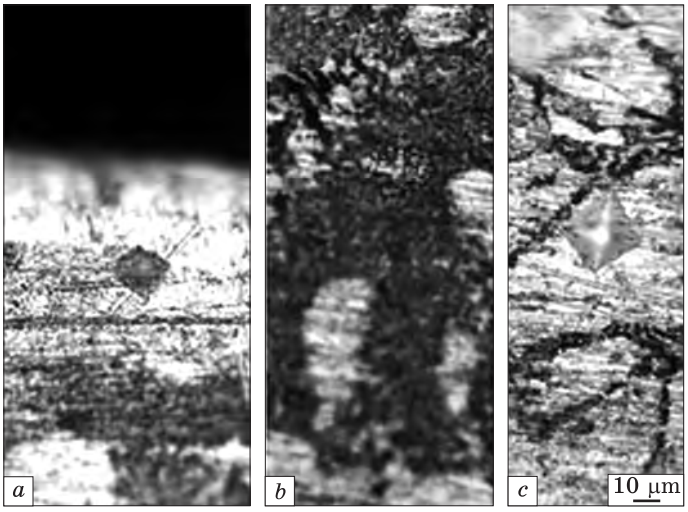

Fig. 2. Microstructure of transverse metallographic section of silumin irradiated by intense pulsed electron beam (E_s = 35 J/cm^2): *a* — silumin structure near the irradiation surface; *b* — eutectic at 70 μm distance from the surface; *c* — indentation in aluminium grain at 70 μm distance

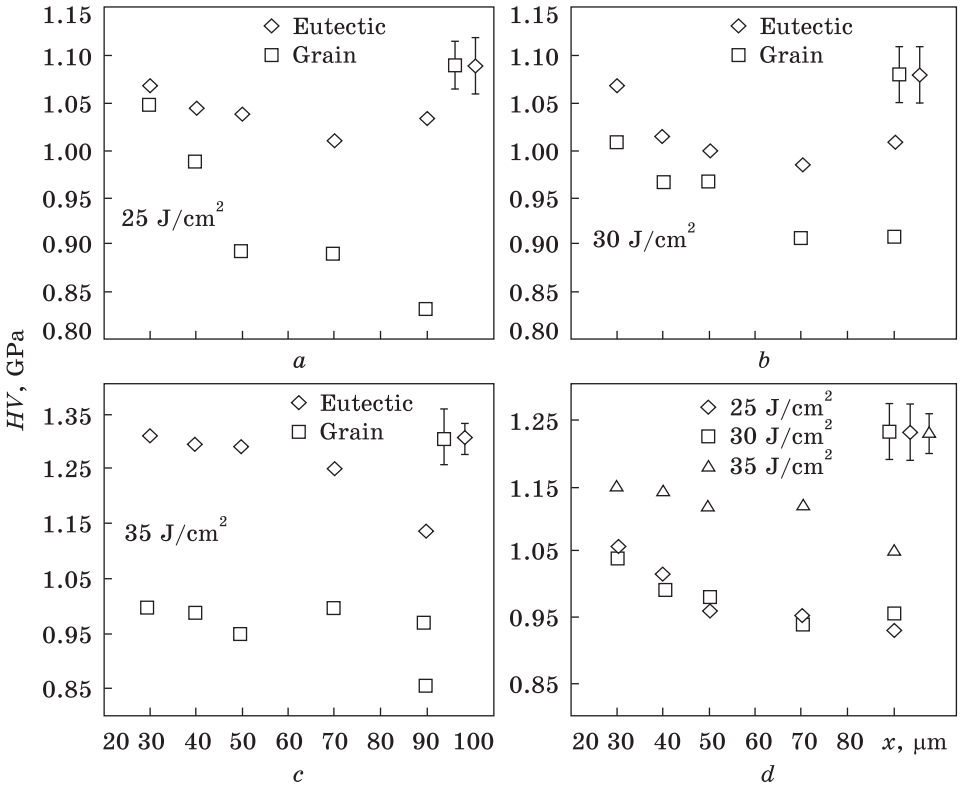

Fig. 3. Dependences of microhardness value distribution in the grains and in the eutectic of silumin on the distance from the modified surface (*a* — 25 J/cm²; *b* — 30 J/cm²; *c* — 35 J/cm²; *d* — on the average in the material)

layer, it has the minimum values irrespective of the treatment regime. The movement deep into the material results in the non-monotonous increase in the plasticity parameter. It should be noted that the plasticity parameter has the minimum values in the eutectic in the treatment regime of 35 J/cm². Moreover, the plasticity parameter value is larger in grains than in eutectic irrespective of the treatment regimes.

The tribological properties of modified silumin are characterized by the wear intensity (the parameter inverse to wear resistance) and friction coefficient. Simultaneously with the microhardness increase, the decrease in the friction coefficient and wear intensity is observed in the irradiated samples.

At an irradiation parameter E_s = 35 J/cm², the friction coefficient varies relative to as-received sample (μ = 0.45 relative to 0.47). Different data are obtained on irradiation with energy density of electron beam E_s = 15 J/cm²: the wear coefficient relative to as-received sample decreased by 21% and amounted to 0.37.

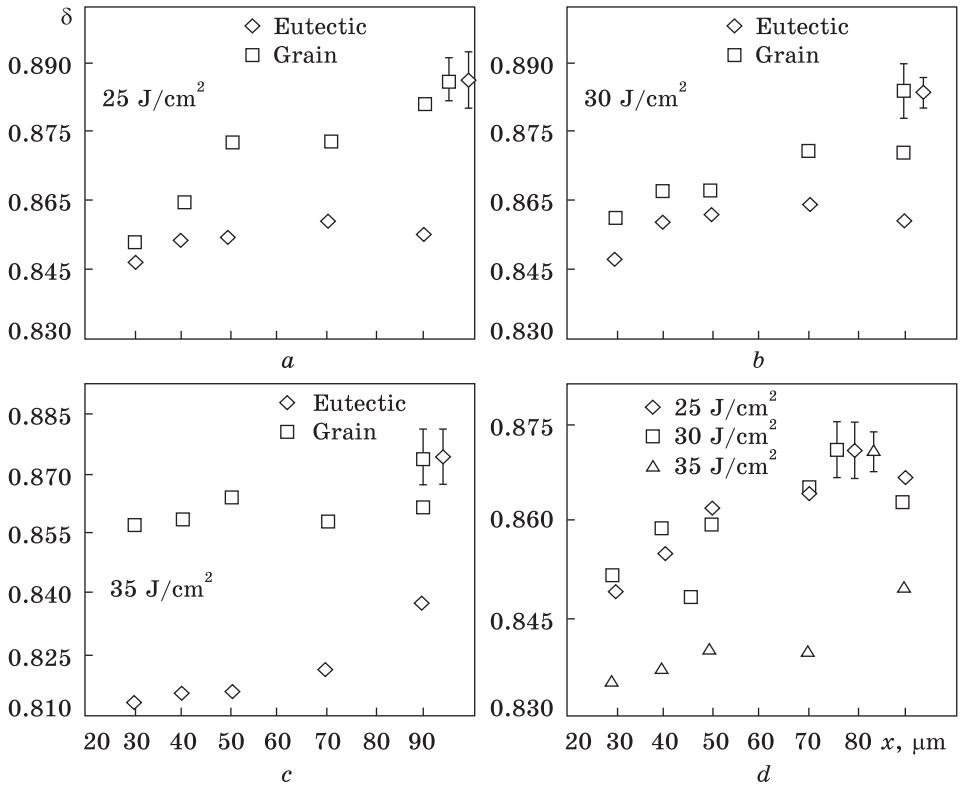

Fig. 4. Dependence of plasticity parameter in the grains and eutectic on the distance from the modified surface of silumin samples subjected to electron beam treatment (*a* — 25 J/cm²; *b* — 30 J/cm²; *c* — 35 J/cm²; *d* — on overage in the material)

The wear intensity of irradiated sample decreases many times and is practically independent on triboloading parameters ($I = 2.7 \cdot 10^{-3}$ relative to $0.78 \cdot 10^{-3}$ mm³/(N·m) at $E_s = 35$ J/cm² and $0.93 \cdot 10^{-3}$ mm³/(N·m) at $E_s = 15$ J/cm²). In our opinion, the reason for it should be the development of seizure and pitting processes of hardening particles characteristic of Al-alloys and its suppression due to irradiation-caused modification of the surface layer structure.

The time of running for as-received sample, the production of friction coefficient value at the set regime of change, is much longer (in the terms of friction path it is not less than 0.003 km). On the other hand, the friction coefficient value itself for as-received samples and after irradiation (at $E_s = 35$ J/cm²) is practically identical. In the authors' opinion, the primary reason of it is the decrease in the slip velocity that due to the decrease in the friction heating should decrease in the intensity of the development of seizure and pitting processes of the hardening particles.

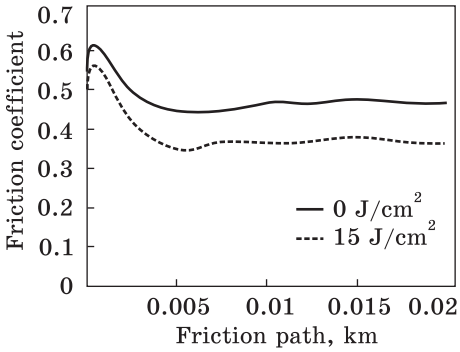

Fig. 5. Dependence of friction coefficient μ on the time of tribological tests in the cast state silumin and after irradiation with an intense electron beam (15 J/cm^2)

For the comparison, the graph of change in the wear coefficient of silumin irradiated by the smaller dose (E_s = 15 J/cm^2), for which the decreased μ value corresponds to the decreased wear intensity as compared to the unirradiated material (compare $I = 0.93 \cdot 10^{-3}$ mm^3/(N·m) relative to 2.7×10^{-3} mm^3/(N·m), is shown in Fig. 5.

The additional information about the causes of the regularities being observed was obtained from the analysis of tribotracks of the tested samples. In the case of the irradiated sample (E_s = 35 J/cm^2), the tribotrack width amounted to 500 μm and its depth was less than 12.1 μm. The measurements of the indentation area showed that the irradiation resulted in decrease of the indentation area from 8.52 μm^3 (cast state) to 2.47 μm^2 (E_s = 35 J/cm^2). For the smaller dose of electron-beam treatment (E_s = 15 J/cm^2), the investigation area amounted to 2.95 μm^2, and the maximum depth was less than 14.3 μm.

In addition to it, the studies of friction track surfaces were performed. It is seen that the friction surface of the unirradiated sample

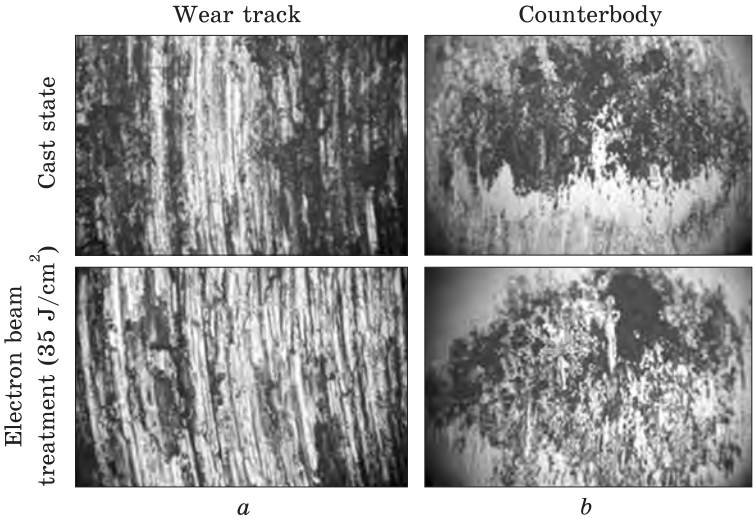

Fig. 6. Optical images of friction tracks (a) and counterbody (b) for the cast-state silumin and after irradiation with an intense pulsed electron beam

looks less homogeneous and a large number of dark regions testifies in favour of the development of seizure and pitting processes. These phenomena are displayed in the irradiated sample of silumin to a far lesser extent. The analysis of counterbody surfaces shows that, in tribotests, the processes of transfer of wear products develop; the counterbody for the unirradiated sample contains a large number of dark regions being the consequence of the wear product sticking (Fig. 6, *b*). The process is displayed in the far lesser extent on the surface of counterbody.

It follows from the analysis of wear track profiles of silumin that, in tribotechnical tests of the cast material, the wear tracks are formed, they have the essentially larger dimensions and a large drop of track depth.

It is evident that the substantial increase in microhardness and tribotechnical properties of silumin mentioned above is caused by the modification of the elemental and phase composition as well as the state of defect substructure of silumin surface layer initiated by high-speed thermal treatment taking place in the irradiation of the material by intense pulsed electron beam [43–48].

3.2. Atomic-Force Microscopy of Silumin Subjected to EBT

The image of the initial sample profile obtained by the atomic-force microscopy is shown in Fig. 7. The presence of the dendritic granular structure and intergranular eutectic is seen. The grain boundaries have the inclusions of intermetallides consisting mostly of copper, manganese and nickel, which were revealed by the methods of scanning electron microscopy. The roughness of the silumin initial sample amounts to ≈50 nm.

The images of the sample profiles treated by different regimes are presented in Figs. 8 and 9.

With E_s = 20 J/cm^2, the fine-grained cellular structure as well as eutectic and partly remelted grain boundary (designated by digits and arrow in Fig. 8, *a*) are formed in silumin. The intermetallides in the structure of the treated layer are absent. The inclusions of the second phases in eutectic have the average dimensions 1–5 μm. The roughness for the treated layer R_a equals to 27 nm, while for the substrate, equals to 57 nm.

The structure of sample cross-section treated by the electron beam with

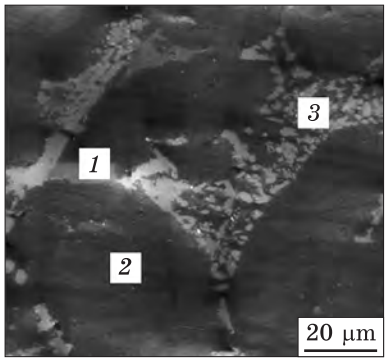

Fig. 7. Atomic-force microscopy of the initial sample: *1* — intergranular boundary, *2* — dendritic grain, *3* — intergranular eutectic

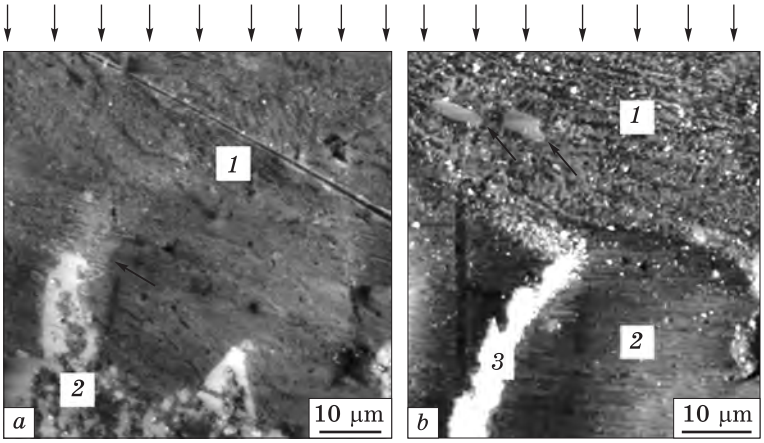

Fig. 8. Atomic-force microscopy of silumin treated with electron beam possessing energy density of 20 J/cm^2 (*a*) and 25 J/cm^2 (*b*). Arrows designate the direction of electron beam effect

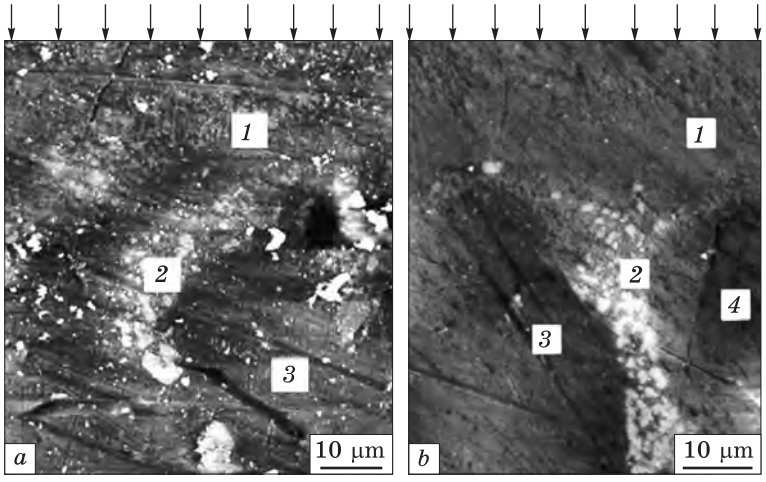

Fig. 9. Atomic-force microscopy of silumin after EBT with E_s = = J/cm^2 (*a*) and 35 J/cm^2 (*b*), where arrows show the direction of electron beam effect. (*a*) *1* — directionally recrystallized grains situated in the treated layer, *2* — incompletely melted grain boundary, *3* — grain body. (*b*) *1* directionally recrystallized grains situated in the treated layer, *2* — intergranular eutectics, *3* and *4* — dendritic grains

energy density of electron beam of 25 J/cm^2 presented in Fig. 8, *b* shows that the treated layer contains the fine-grained structure and the grains with grain boundary (designated by the digits). The roughness of the treated layer R_a is 27 nm, and the roughness of substrate is 45 nm. In the structure of the treated layer, the partially transformed boundaries

of grains that were not completely recrystallized (designated by white arrows in Fig. 8, *b*) are observed as well.

In the layer after EBT with E_s = 30 J/cm^2, the directionally recrystallized grains (Fig. 9, *a*) are revealed. The incompletely melted grain boundary is designated by *2*. The roughness of the treated layer R_a equals to 33 nm, and the roughness of substrate equals to 51 nm. The layer structure after EBT with E_s = 35 J/cm^2 involves the treated layer *1*, the grain boundary *2* and grain solids *3* and *4* (Fig. 9, *b*). The roughness of the treated layer R_a = 17 nm, while the roughness of substrate equals to 45 nm.

Depending on the energy density of electron beam, the average roughness of the treated layer R_a varies from 17 to 99 nm, and that of the substrate varies within the range from 30 to 77 nm. The largest average value of the layer roughness R_a being equal to 99 nm was obtained in the sample treated by the electron beam with energy density of electron beam of 10 J/cm^2, the least one — 17 nm with energy density of 35 J/cm^2.

The results obtained by means of atomic-force microscope make it possible to consider that the effective regimes are the regimes of E_s from 25 to 35 J/cm^2. In comparison with the other regimes, they are characterized by the formation of fine-grained cellular structure and they have the least roughness of the treated layer (of 17–33 nm) and substrate (of 45–57 nm) as well. The selection of the optimal regime of treatment according to atomic-force microscopy correlates to the selected regimes according to the results of microhardness measurement.

3.3. Fine Structure and Phase Composition of the Surface Layers of Silumin after EBT

It was shown by the methods of scanning electron microscopy that silumin was a multiphase aggregate, whose structure was presented by the solid solution grains on aluminium base, the grains of eutectic Al–Si, the inclusions of the initial silicon, and intermetallides, whose dimensions and shape varied in the rather wide ranges (Fig. 10). The presence of intermetallides results in the decrease in crack resistance of silumin [49–52]. Another unfavourable factor of cast alloy structure is the presence of micropores (Fig. 10, *c*).

The results of the quantitative x-ray structural analysis are shown in Table 2. It is seen that the base phases of the tested material, as could be expected, are the solid solutions based on aluminium and silicon in the alloy being tested are close to those of pure elements and it indicates to the layering of these elements on crystallization of the alloy.

The results of the studies of the phase composition and the state of crystal lattice of silumin surface layer after EBT presented in Table 3

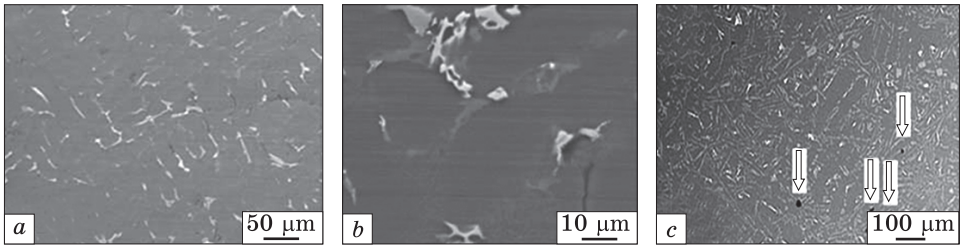

Fig. 10. SEM images of the structure of silumin in the cast state: *a*, *b*, *c* correspond to different scales; arrows (*c*) designate micropores

indicate that three phases are present in the surface layer. The crystal lattice parameters of the revealed phases differ from the tabular values for pure elements. The fact can be indicative of formation of solid solution based on aluminium and silicon taking place at high-speed crystallization of the melted layer.

The smaller values (relative to tabular ones) of Al, silicon, and AlSi-phase crystal-lattice parameters may be indicative of the alloying of the phases by the elements with atomic dimensions less than those for Al and Si: $R_{Al} = 0.143$ nm, $R_{Si} = 0.132$ nm, $R_{Cu} = 0.128$ nm, $R_{Fe} = 0.126$ nm, $R_{Ni} = 0.124$ nm [53].

The electron-microscope image of the transverse metallographic section structure presented in Fig. 11 enables one to speak about the fact that the irradiation by the intense pulsed electron beam results in the cast material in the surface layer whose thickness varies within 40–60 μm for the indicated parameters of electron beam (25 J/cm^2; 150 μs; 3 pulses).

Table 2. **Results of x-ray structural analysis of silumin in the cast state**

Phase	Relative content, wt.%	Lattice type (space group)	Lattice parameter, nm		Atomic radius, nm
			tabular, a_0	in alloy, a	
Al	84.2	*Fm3m*	0.4050	0.40484	0.143
Si	12.3	*Fm3ms*	0.54307	0.54265	0.132

Table 3. **Results of x-ray structural analysis of silumin surface irradiated with intense pulsed electron beam**

Phase composition	Relative content, wt.%	Lattice parameter, nm	
		irradiated	tabular [53]
AlSi	53.13	0.40412	
Al	38.29	0.40419	0.40494
Si	8.58	0.54191	0.54307

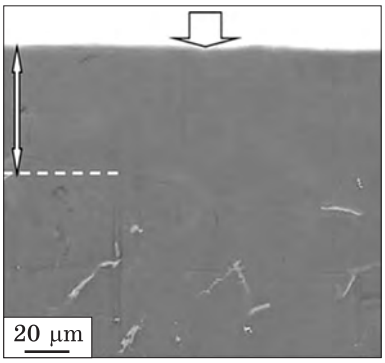

Fig. 11. Electron microscope image of transverse metallographic section structure of silumin after EBT (E_s = 25 J/cm^2). The arrows designate the irradiation surface and thickness of the surface layer, in which the initial inclusions of the second phase are not revealed *via* SEM methods

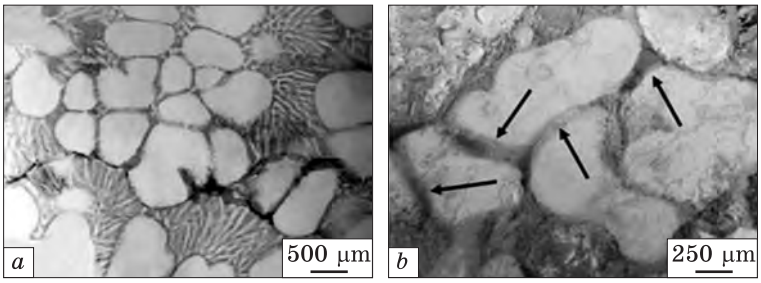

Fig. 12. Electron microscope image of cellular crystallization structure of silumin surface layer after EBT (E_s = 25 J/cm^2). Arrows (*b*) designate the second phase interlayers located at the cell's interface boundary

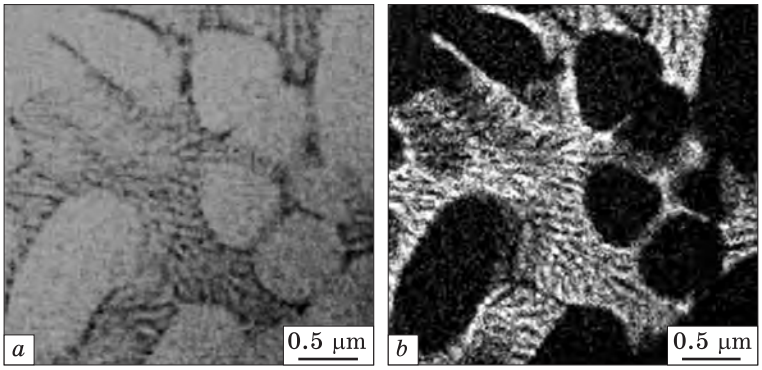

Fig. 13. The structure of silumin surface layer obtained in the characteristic x-ray radiation of Al (*a*) and Si (*b*) atoms

The structure of the surface layer modified by the electron beam was studied in more detail by transmission electron microscopy (TEM) methods of thin foils fabricated from the transverse cross-section of the samples.

In the surface layer, the cells of two types (Fig. 12) are formed. First, there are the cells whose volume is free from the second phase

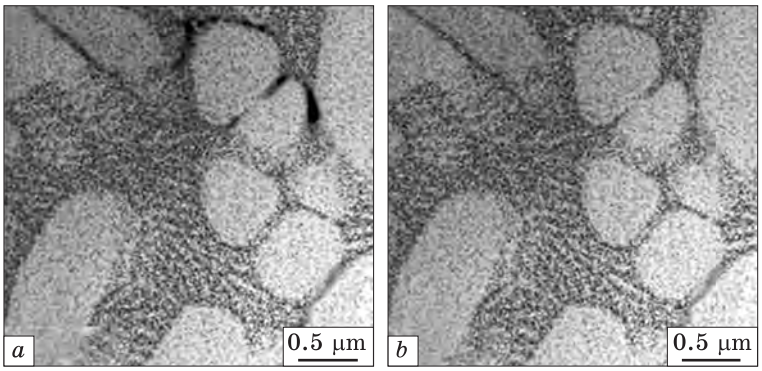

Fig. 14. Surface layer structure of silumin foil region formed as a result of superposition of (*a*) bright field image and the image obtained in the characteristic x-rays of silicon atoms, (*b*) bright field image and the images obtained in the characteristic x-rays of silicon, copper, and nickel atoms

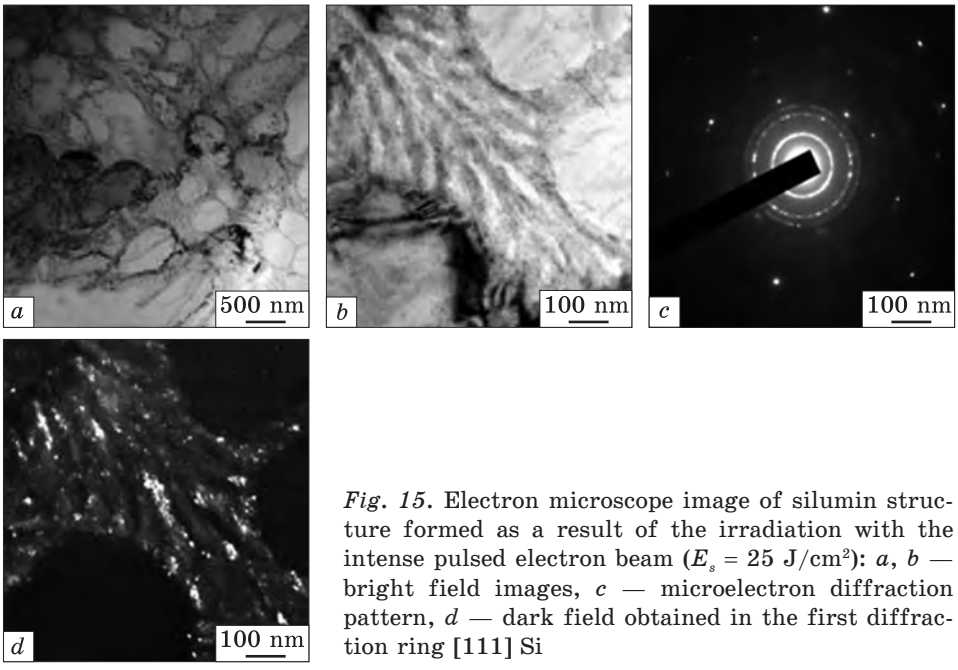

Fig. 15. Electron microscope image of silumin structure formed as a result of the irradiation with the intense pulsed electron beam (E_s = 25 J/cm^2): *a*, *b* — bright field images, *c* — microelectron diffraction pattern, *d* — dark field obtained in the first diffraction ring [111] Si

precipitates. In some instances, the round shaped particles located chaotically are observed in the volume of these cells. Secondly, the cells in whose volume the structure of lamellar eutectic (Fig. 12, *a*) is observed. Note that the cells of first type at the given irradiation regime are the predominant type of the structure of the surface layer ≈10 μm thick. At the larger distance from the irradiation surface, the mixed type struc-

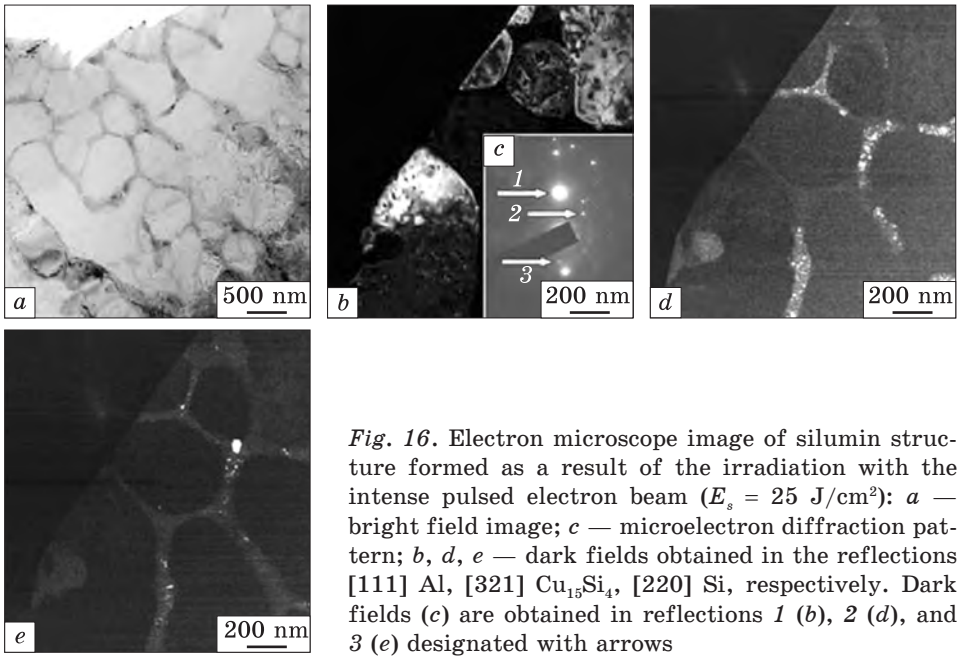

Fig. 16. Electron microscope image of silumin structure formed as a result of the irradiation with the intense pulsed electron beam (E_s = 25 J/cm^2): *a* — bright field image; *c* — microelectron diffraction pattern; *b*, *d*, *e* — dark fields obtained in the reflections [111] Al, [321] $Cu_{15}Si_4$, [220] Si, respectively. Dark fields (*c*) are obtained in reflections *1* (*b*), *2* (*d*), and *3* (*e*) designated with arrows

ture presented by the cells of first and second type is formed. The cells are separated by the thin interlayers of the second phase; the interlayer dimensions are less than 100 nm (Fig. 12, *b*).

The studies of the elemental composition of first type and second type cells (Figs. 13, 14) were performed by the methods of x-ray spectrum analysis (method of mapping) [54].

It is established that the volume of first type cells is enriched by Al atoms (Fig. 13a), that is it represents the Al-based solid solution. The second type cells are formed by the alternating plates parallel to each other and enriched by atoms of aluminium (Fig. 13, *a*) and silicon (Fig. 13, *b*), *i.e.* they represent the cells of Al–Si alloy eutectic. The transverse dimensions of the silicon and aluminium interlayers vary within the range of 40–60 nm. Si, Cu, Ni, and Fe atoms (Fig. 14) enrich the second phase interlayers located at the cells' interface.

Figure 15 shows the results of TEM investigation into the lamellar eutectic structure. The analysis of microelectron diffraction pattern (Fig. 15, *c*) gives grounds for concluding that the plates (Fig. 15, d) are formed by silicon. The silicon plates are polycrystals with crystal dimensions of 5–10 nm. The ring structure of microelectron diffraction pattern (Fig. 15, *c*) indicates the nanocrystalline structure of silicon plates.

Figure 16 illustrates the TEM analysis results of cellular crystallization structure of silumin. The analysis of microelectron diffraction

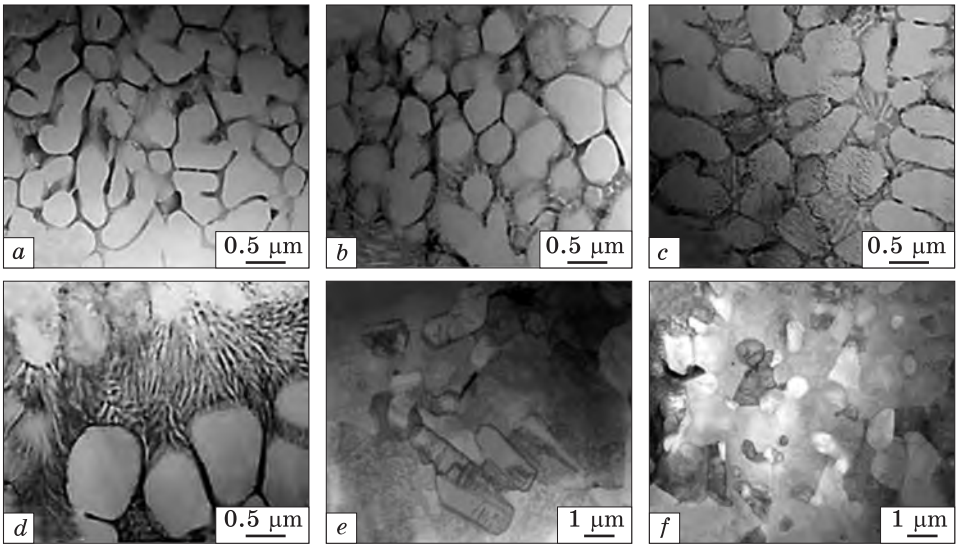

Fig. 17. TEM image of silumin structure after EBT (E_s = 25 J/cm^2): *a* — structure of 5 μm thick layer adjoining to the irradiation surface; *b*–*f* — structures of layers located at distances of x = 15, 30, 50, 120, 200 μm from the irradiation surface, respectively

pattern presented in Fig. 16 depicts that the cells of speed crystallization are formed by the solid solution based on aluminium (Fig. 16, *b*). The interlayers separating the crystallization cells are the multiphase formations. The analysis of microelectron diffraction patterns obtained from the bulks of foil containing the interlayers enabled one to identify the particles of following phases: $Cu_{15}Si_4$ (Fig. 16, *d*), silicon (Fig. 16, *e*), copper, and Al_4Cu_9 in the interlayers.

The layer-by-layer TEM analysis of the silumin structures revealed the graded structure of the surface layers (Fig. 17). The layer of the thick of 8–10 μm adjoining to the irradiation surface has a cellular structure, the cells' boundaries are the second phase interlayers whose thickness is less than 100 nm (Fig. 17, *a*). The grains of eutectic are absent.

With the larger distance from the irradiation surface, the cells (grains) with the lamellar substructure (eutectic) (Fig. 17, *b*–*d*) are found in the cellular crystallization structure. The relative content of such grains increases with the increase in the distance from the irradiation surface. The first grains of eutectic are identified in the layer located at the depth of ≈15 μm. As the distance from the irradiation surface increases, the relative content of eutectic grains increases. Islands and interlayers between the cells of high-speed crystallization of aluminium locate the grains of eutectic. The presence of eutectic grains is indicative of the existence of the local regions with relatively high concentration (≈12 at.%) of silicon atoms in the surface layer of the

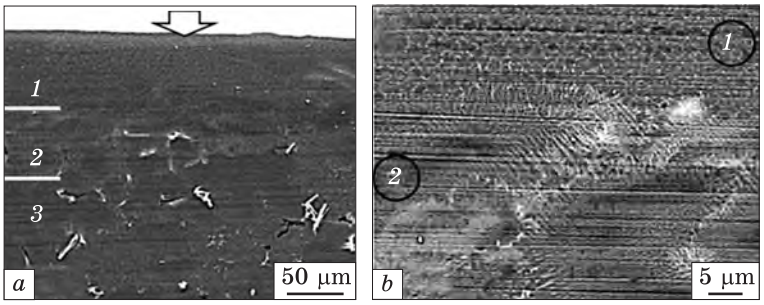

Fig. 18. Electron microscope image of transverse metallographic section structure of silumin sample after EBT (E_s = 35 J/cm^2), where the irradiated surface (marked with an arrow), surface layer (*1*), transition layer (*2*), and layer of thermal effect (*3*) are designated

material. The dimensions of eutectic grains are close to those of solid solution based on aluminium (crystallization cells). The transverse dimensions of eutectic plates vary within the range of 25–50 nm.

The inclusions of intermetallides of cast origin located in the cellular crystallization structure are found at the depth of 50–70 μm. The inclusions of intermetallides occur as the centres of cellular crystallization.

The layer of silumin, in which only Al melts and the initial inclusions of Si and intermetallides are present, is detected at 80–90 μm distance from the irradiation surface. In this case, the cells of high-speed crystallization of Al are observed in the structure. The grains of lamellar eutectic of submicron dimensions are absent. At a distance of 100–200 μm from the irradiation surface, the cellular crystallization structure is not revealed (Fig. 17, *e*, *f*).

The study of silumin surface after EBT with E_s = 35 J/cm^2 by the methods of scanning electron microscopy failed to show the essential differences from the structure being formed on irradiation with E_s = 25 J/cm^2. However, there are some features need to be considered. It is established that the dimensions of the melted layer increase with the growth of energy density of electron beam.

At the energy of electron beam of 35 J/cm^2, the thickness of the modified surface layer, in which the initial inclusions of silicon and intermetallides fail to be detected by SEM method, increases from 70 to 100 μm (Fig. 18, *a*).

By morphology of the defect substructure, three layers can conditionally be distinguished: the surface layer, transition layer, and the layer of thermal effect (Fig. 18, *a*). The surface layer has the structure of cellular crystallization formed at a high-speed cooling of the material from the molten state (Fig. 18, *b*, layer *1*). In the layer, the initial inclusions of the second phase fail to be detected by SEM methods. The transition layer is characterized by the presence of the initial inclusions of

the second phase that are the centres of Al crystallization (Fig. 18, *b*, layer *2*).

Phase composition and crystal lattice state of silumin modified by the intense pulsed electron beam were studied by the methods of x-ray structural analysis, the results of which are given in Table 4.

As one can see from the data in Table 4, the irradiation of silumin by electron beam results in the formation of two solid solutions based on aluminium designated in Table as AlSi and Al, the precipitation of copper aluminide $AlCu_2$ and silicon. The crystal lattice parameter of AlSi solid solution is less than that of pure aluminium being equal to 0.40494 nm [53]. It is caused by the fact that the atomic radius of silicon (0.132 nm) is smaller than that of aluminium (0.143 nm) [53] and consequently, the substitution of aluminium atoms by silicon will result in the decrease in the crystal lattice parameter of AlSi solid solution. The crystal lattice parameter of the second phase based on aluminium solid solution is larger than that of pure aluminium. It is connected

Table 4. **Results of x-ray structural analysis of silumin modified with intense pulsed electron beam**

Phase composition	Relative content, wt.%	Lattice parameter, nm		Coherent scattering area, nm	$\Delta d/d$, 10^{-3}
		a	*c*		
AlSi	40.8	0.40435			
Si	4.1	0.54274		34.48	2.311
Al	40.7	0.40508			
$AlCu_2$	14.4	0.40311	0.57492	29.83	0.926

Table 5. **Elemental composition of different regions (*1–9*) of cellular substructure of silumin surface layer after treatment by means of the electron beam with energy density of 25, 30 or 35 J/cm²**

Element	Concentration, at.%								
	Number of region analysed *via* micro-x-ray spectroscopy								
	25 J/cm²				30 J/cm²			35 J/cm²	
	1	*2*	*3*	*4*	*5*	*6*	*7*	*8*	*9*
Mg	0.32	0.81	0.44	1.28	0.0	0.14	0.0	0.0	0.0
Al	90.14	89.41	86.83	89.82	92.14	90.97	91.77	91.1	92.83
Si	7.15	6.88	10.36	6.13	5.86	6.25	6.17	3.68	4.69
Ti	0.11	0.13	0.11	0.08	0.04	0.05	0.01	0.13	0.25
Mn	0.02	0.01	0.02	0.02	0.0	0.01	0.0	0.04	0.02
Fe	0.11	0.24	0.12	0.14	0.14	0.07	0.12	0.59	0.1
Ni	0.2	0.6	0.28	0.36	0.37	0.61	0.41	2.02	0.45
Cu	1.94	1.9	1.83	2.17	1.45	1.9	1.53	2.44	1.67

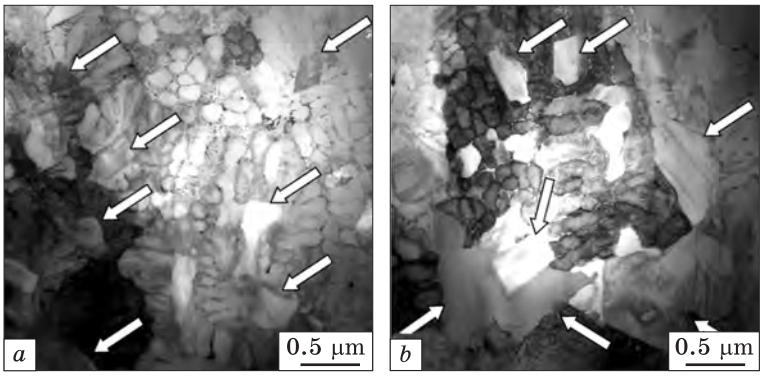

Fig. 19. Structure of silumin irradiated with an intense pulsed electron beam (E_s = = 35 J/cm^2), where layers at the depths of 70 μm (*a*) and 90 μm (*b*) are imaged. The arrows designate inclusions of the cast origin (initial state)

with the dissolution of intermetallides particles and the enrichment of solid solution by atoms of metals whose atomic radius is larger than that of aluminium. The crystal lattice parameter of Si precipitations is less than that of the tabular value (a_{Si} = 0.54307 nm) [53]. It means that, in the process of crystallization, the solid solution based on silicon is formed, and, in it, the atoms of copper, nickel and iron can be present because the atomic radii of these elements are less than that of silicon. The relative content of silicon in the modified layer of silumin is comparatively small and by magnitude is close to the value obtained by the methods of x-ray spectroscopic analysis.

Table 5 illustrates the elemental composition of different parts of silumin surface layer after EBT. It may be noted that silumin irradiation by the intense pulsed electron beam in the regime of surface layer melting results in: first, homogenization of the elemental composition of the surface layer; secondly, the decrease in the concentration of silicon atoms in the surface layer being intensified with the growth of energy density of electron beam.

As it has already been noted, the cellular crystallization structure, as the distance from the surface of treatment increases, transits to the structure of the mixed type, in which the partially dissolved inclusions of the cast origin (Fig. 19) are present along with the cells. The analysis of the transition type showed the absence of the lamellar form inclusions in the structure. In most cases, the inclusions have a quasi-equiaxed form (Fig. 19, *a*). The statement is true for both silicon particles as well and intermetallide particles. It should be noted that the globularization of silicon particles and intermetallides should substantially increase in the plastic properties not only of the modified layer but also the material overall.

3.4. Mechanisms of Electron-Beam Effect on Silumin

The reason for the initiation of the columnar crystallization (Figs. 12, 17) may be the thermocapillary instability, which arises from the presence of temperature gradient in the liquid layer, and it results in the formation of vortices (Fig. 20) and the displacement of the second phase particles to the boundary of columns [55].

The mechanism of the instability and formation of vortices can be understood from the following arguments. Let us consider the half-space $z < 0$ (Fig. 20). The temperature of the material is maximum on the surface, and it decreases at the depth. Suppose the surface of liquid is perturbed with analytical form $\eta(x,t) = A_0\exp(\alpha t)\cos(kx)$, where α — exponent, η — displacement of liquid particles from the equilibrium position, A_0 — amplitude of the displacement, k — wave number. Then, for the vertical component of velocity, from the kinematical boundary condition, it follows the expression $V_z(t,x,0) = \alpha A_0\exp(\alpha t)\cos(kx)$. The exponent α depends on wave number k: $\alpha = \alpha(k)$. In literature on the analysis of instabilities, the value α is still called the growth rate, since the time derivative of $\exp(\alpha t)$ at $t \approx 0$ is equal to α. When $\alpha > 0$, the harmonic oscillation amplitude of liquid increases exponentially resulting in the instability. The value α is called increment (decrement), if $\alpha > 0$ ($\alpha < 0$). For the horizontal velocity component, using the continuity condition, we obtain $V_z(t,x,0) = \dot{\eta} = \alpha A'(z)\exp(\alpha t)\sin(kx)/k$. For distribution of temperature, suppose that temperature decreases with increasing z. In the regions where $V_z > 0$, the temperature increases. When $V_z < 0$, the temperature decreases because the cold substance is carried out from the depth. The temperature perturbation we shall represent in terms of $T(t,x,0) = -\Theta(t,z)\cos(kx)$, where $\Theta(t,z)$ is amplitude of the present perturbation, and surface tension coefficient $\sigma(t,x,z) = \sigma_0 + \sigma_T\Theta(t,z)\cos(k,x)$, σ_0— surface tension at room temperature, σ_T — temperature coefficient of surface tension. For shear stress, $f_x = \partial\sigma/\partial x - \sigma_T\Theta(t,z)\sin(kx)$. Shear stress acts in a direction parallel to horizontal velocity, therefore, the velocity increases. The amplitude growth effect consists in it, and it means that instability develops. This diagram is true on condition that $\alpha > 0$, for the opposite case ($\alpha < 0$), the system will be stable and vortices twist in the opposite direction resulting in the damping.

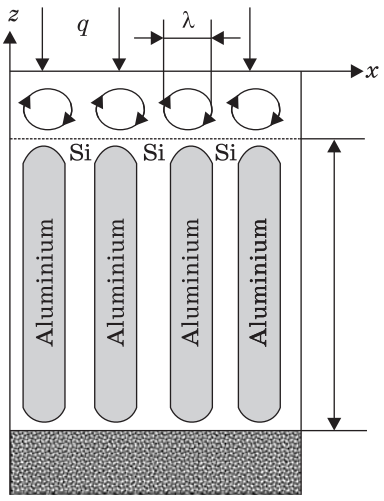

Fig. 20. Scheme of electron-beam effect on silumins

As in Ref. [56], we shall model the heat effect of electron beam using the enthalpy approach. The advantage of the approach is that it enables to take into account the first-order phase transitions without invoking the additional conditions. Consider the electron beam effect (with surface energy density E_s) on flat-plate-shaped sample with thickness h. Since we are interested in the temperature depth distribution of the sample, we restrict ourselves to the solution of one-dimensional problem of heat conduction. We direct the axis Z inside the plate. The flow of electrons affects the surface $z = 0$ during time t_0 and on the rear side of the plate $z = h$ the heat blow is absent. Heat condition equation in this case reads as

$$\rho \frac{\partial H}{\partial t} = \frac{\partial}{\partial z}\left(\lambda \frac{\partial T}{\partial z} \right), \tag{1}$$

where H — enthalpy, ρ — density, λ — heat conduction coefficient, T — temperature. Phase transitions under the electron-beam effect are taken into account as follow:

$$\rho H(T) = \begin{cases} \rho_S C_S T, & T < T_L; \\ \rho_L (L_L / \Delta T_L) T, & T_L \le T \le T_L + \Delta T_L; \\ \rho_L C_L T, & T_L + \Delta T_L \le T < T_V; \\ \rho_V (L_V / \Delta T_V) T, & T_V \le T \le T_V + \Delta T_V; \\ \rho_V C_V T, & T_V + \Delta T_V \le T; \end{cases} \tag{2}$$

C_p — coefficient of heat capacity; L — specific heat of phase transition; indices S, L and V correspond to the solid, liquid, and vapour phase. The heat flow is set on the surface of the sample ($z = 0$):

$$-\lambda (\partial T / \partial z) = q_0(t); \quad q_0(t) = \begin{cases} E_S / t_0 - \dot{m}(T) L_V, & 0 \le t \le t_0; \\ 0, & t > t_0; \end{cases} \tag{3}$$

$\dot{m}(T) = p_c (1 - \beta) \sqrt{M / (2\pi R T)}$, $p_c = p_0 \exp[L_V M (T - T_V) / (R T T_V)]$, E_S is an electron-beam energy density, M is a molar mass, R is universal gas constant, p_0 is a pressure at T_V, and β is a constant.

At the boundary ($z = h$),

$$\partial T / \partial z = 0. \tag{4}$$

The initial temperature $T(0, z) = T_{\text{init}}$ along the entire depth of the plate is $0 < z < h$. Numerical solution of Eqs. (1)–(4) was done *via* the implicit difference scheme by the 'marching' method.

The thermal physical constants of silumin were calculated by the rule of mixture. Table 6 represents the values of the constants. As the conditions of high vacuum were in the experiment, the value of vaporization temperature was calculated according to the Clausius–Clapeyron equation. It amounted to 1270 K.

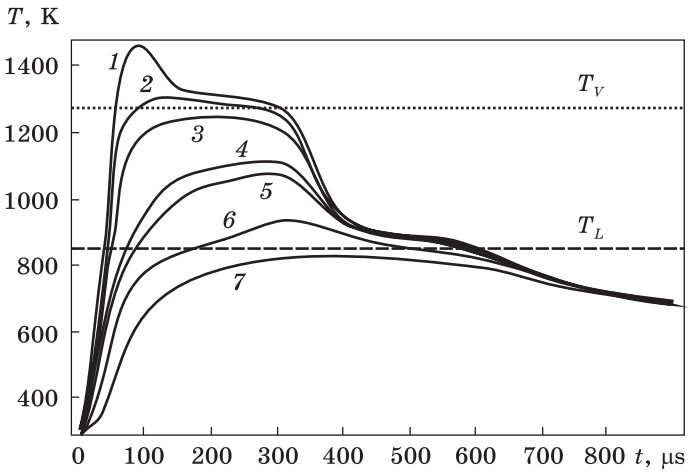

Fig. 21. Time (t) evolution of temperature (T) at different distances (depths) from the irradiated surface (E_s = 35 J/cm^2): 0 (*1*), 10 (*2*), 20 (*3*), 25 (*4*), 30 (*5*), 50 (*6*), and 80 μm (*7*)

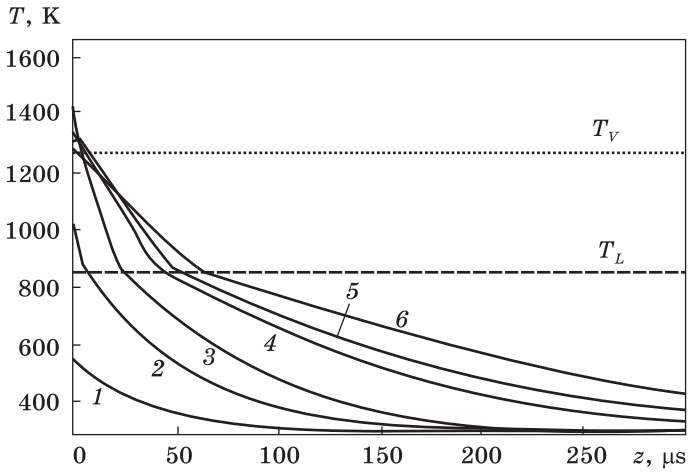

Fig. 22. Temperature *vs.* distance from the irradiated surface at different temporal values: 50 (*1*), 100 (*2*), 150 (*3*), 300 (*4*), 400 (*5*), and 600 μs (*6*)

The time and distance distributions of temperature from the irradiated silumin surface were calculated for electron beams possessing energy densities 15–35 J/cm^2 with pulse duration t_0 = 150 μs.

Figure 21 shows the time distribution of temperature at different distance from the irradiation surface under the electron-beam effect with energy density of 35 J/cm^2. As one can see on the graphs *1*–*6*, after the finishing of pulse effect to the moment of time 300 μs, the cooling rate of substance is insignificant. This is indicative of the presence

of the vapour interlayer holding the high temperatures on the surface. At $t > 300$ μs, the cooling rate increases abruptly, while its values on the surface and at the depths to 20 μm (curves *1–3*) are higher than at the depths from 20 to 50 μm (curves *4–6*). It is indicative of the expansion of the vapour interlayer. Estimation of cooling rate of surface layers has shown that it reaches the values of ~10^6 K/s. At these values of cooling rate, as it has been mentioned earlier in Ref. [56], the structure of cellular crystallization is formed. At the depth of 80 μm (curve *7*), the temperature value is less than the temperature of eutectic.

Analysis of temperature dependence on coordinates (Fig. 22) has shown that silumin is still in the solid state (curve *1*) at a time moment of 50 μs. The electron-beam action, in this case, decreases, in addition, to the generation of thermoelastic wave [55] besides the heating. At $t = 100$ μs (curve *2*), the material is in the molten state within the interval 0–10 μm. Here, the convective flow of the melt starts to develop. To the moment of time of finishing of pulse action (curve *3*), in the interval from 0 to 15 μm, the substance is in the gaseous state, while the thickness of the evaporated interlayer increases to the moment of time of 300 μs (curve *4*). Then, the gradual equalizing of temperature to depth (curves *5* and *6*) is observed.

Table 6. **Thermal physical characteristics of silumin [55]**

Unit symbol, unit of measurement	Quantity value	Description
T_L, K	850	Eutectic temperature
T_V, K	1270	Temperature of vaporization
ρ_S, kg/m^3	2656	Density of silumin in solid state
ρ_L, kg/m^3	2398	Density of silumin in liquid state
C_S, J/(kg·K)	880	Specific heat capacity in solid state
C_L, J/(kg·K)	1160	Specific heat capacity in liquid state
λ_S, W/(m·K)	200	Heat conduction in solid state
λ_L, W/(m·K)	86	Heat conduction in liquid state
L_L, kJ/kg	385	Specific heat of melting
L_V, kJ/kg	10444	Specific heat of vaporization

Table 7. **Calculated and experimental melted layer thicknesses of silicon (d_{Si}), aluminium (d_{Al}), and silumin specimen (d) irradiated with high-intensity electron beams (of different densities, E_s) for pulse duration of 150 μs**

E_s, J/cm^2	d_{Si}, μm	d_{Al}, μm	d, μm [57]
15	23	18	23
20	39	39	30
25	54	57	55
35	80		80

The calculations of melting depth (Table 7) showed that the thickness of the melted layer increases with the growth of energy density of electron beam. Its values coincide practically with the experimental ones [57].

We shall use the obtained data on the depth of melting and surface temperature for the estimation of temperature gradient in development of the thermocapillary model of surface cellular structure formation.

For the solution of formulated problem, let us take the rectangular coordinate system (x, y, z) and consider the viscous incompressible heat-conducting liquid that occupies the layer of thickness h on the free surface $z = \eta(x, y, t)$ and absorbs heat. At the values of heat flow of $\sim 10^5$ W/cm^2 used in the experiment, the approximation of the incompressible liquid should be considered as justified in Ref. [58]. After the electron-beam effect, the temperature in the liquid layer profile is $T_0 = T(z)$. Let the wave vector of perturbations be directed in XOY plane. Then, they exponentially depend on the coordinates X, Y, and time: $\propto \exp(\omega t - i(mx + ly))$.

For the study of instability of stationary state, let us linearize Navier–Stokes equation and the equation of heat conduction for temperature $T_0(z) = T(x, y, z, t)$. They will take the forms as follow:

$$\begin{gathered}
\frac{\partial u}{\partial t} = -\frac{\partial p}{\rho \partial x} + \nu\left(\frac{\partial^2 u}{\partial x^2} + \frac{\partial^2 u}{\partial y^2} + \frac{\partial^2 u}{\partial z^2}\right), \\
\frac{\partial v}{\partial t} = -\frac{\partial p}{\rho \partial y} + \nu\left(\frac{\partial^2 v}{\partial x^2} + \frac{\partial^2 v}{\partial y^2} + \frac{\partial^2 v}{\partial z^2}\right), \\
\frac{\partial w}{\partial t} = -\frac{\partial p}{\rho \partial z} + \nu\left(\frac{\partial^2 w}{\partial x^2} + \frac{\partial^2 w}{\partial y^2} + \frac{\partial^2 w}{\partial z^2}\right), \\
\frac{\partial u}{\partial x} + \frac{\partial v}{\partial y} + \frac{\partial w}{\partial x} = 0, \\
\frac{\partial T}{\partial t} + w\frac{dT_0}{dz} = \chi\left(\frac{\partial^2 T}{\partial x^2} + \frac{\partial^2 T}{\partial y^2} + \frac{\partial^2 T}{\partial z^2}\right),
\end{gathered} \tag{5}$$

where u, v, w — components of the perturbed-velocity vector; c — ensity of the melt; p, T — perturbations of pressure and temperature; ν, χ, $\sigma(T)$ — kinematic viscosity, coefficient of heat conduction, and surface tension, respectively. We consider that surface tension depends on temperature by linear law:

$$\sigma = \sigma_0 + \sigma_T(T - T_{\text{init}}), \tag{6}$$

where σ_T — temperature coefficient of surface tension, σ_0 — surface tension at room temperature T_{init}.

The boundary conditions on the surface of the melt, $z = 0$, take the form:

$$-p + 2\nu\rho\frac{\partial w}{\partial z} = \sigma\left(\frac{\partial^2\eta}{\partial x^2} + \frac{\partial^2\eta}{\partial y^2}\right),$$
$$\rho\nu\left(\frac{\partial u}{\partial z} + \frac{\partial w}{\partial x}\right) = \frac{\partial\sigma}{\partial x},\ \rho\nu\left(\frac{\partial v}{\partial z} + \frac{\partial w}{\partial y}\right) = \frac{\partial\sigma}{\partial y}, \tag{7}$$
$$\frac{\partial T}{\partial z} = 0,\ \frac{\partial\eta}{\partial t} = w.$$

At a melt–solid interface ($z = -h$), the conditions of adhesion and impermeability take place [9]:

$$u = v = w = 0,\ T = 0. \tag{8}$$

The gradient of surface tension along the X and Y axes is given by

$$\frac{\partial\sigma}{\partial x} = \frac{\partial\sigma}{\partial T}\left(\frac{\partial T}{\partial x} + a\frac{\partial T_0}{\partial z}\eta_x\right),\ \frac{\partial\sigma}{\partial y} = \frac{\partial\sigma}{\partial T}\left(\frac{\partial T}{\partial y} + a\frac{\partial T_0}{\partial z}\eta_y\right). \tag{9}$$

Here, the parameter is an introduced for comparing the dispersion equations obtained in [59] at $a = 0$ and in [24] at $a = 1$. Suppose $\sigma_0 = 0$ and $a = 0$, $\sigma_T \neq 0$, then, we obtain the problem of thermocapillary instability with undeformed flat boundary (Pirson problem). We search the solution of Eqs. (5) in terms of

$$\begin{aligned}
u(x,y,z,t) &= U(z)\exp(\omega t - i(mx + ly)),\\
v(x,y,z,t) &= V(z)\exp(\omega t - i(mx + ly)),\\
w(x,y,z,t) &= W(z)\exp(\omega t - i(mx + ly)),\\
P(x,y,z,t) &= P(z)\exp(\omega t - i(mx + ly)),\\
T(x,y,z,t) &= T(z)\exp(\omega t - i(mx + ly)),\\
\eta(x,y,t) &= \eta_0\exp(\omega t - i(mx + ly)),
\end{aligned} \tag{10}$$

where $U(z)$, $V(z)$, $W(z)$, $P(z)$, $T(z)$, η_0 are the perturbation amplitudes of velocity, pressure, temperature, and surface, respectively; $\mathbf{k} = (l, m)$ is a wave vector, i is an imaginary unit. Substituting Eq. (10) into Eqs. (6)–(8), we obtain the following set:

$$P(z) = i\frac{\rho\nu}{k^2}\left(W'''(z) - k_1^2W'(z)\right),\ W''(z) - k_1^2W'(z) - \frac{1}{\rho\nu}P'(z) = 0,$$
$$T''(z) - k_2^2T(z) - G_0W(z)/\chi = 0. \tag{11}$$

where $k_1^2 = \omega/\nu + k^2$, $k_2^2 = \omega/\chi + k^2$, $G_0 = dT_0/dz$. After the transformation, both equations of the system (11) read as

$$W^{IV}(z) - (k^2 + k_1^2)W''(z) + k^2k_1^2W(z) = 0,$$
$$T''(z) - k_2^2T(z) - (G_0/\chi)W(z) = 0. \tag{12}$$

The solutions of the set (12) are as follow:

$$W(z) = A_1 \exp(kz) + A_2 \exp(k_1 z),$$
$$T(z) = C\exp(k_2 z) - (G_0/\omega)[A_1 \exp(kz) - A_2 \delta \exp(k_1 z)],\ \delta = \nu/(\chi - \nu), \quad (13)$$

where A_1, A_2, C are integration constants. Obtaining the dependences (13), we supposed that $h \to -\infty$. In this case, they satisfy the boundary conditions (8). The constant C was found from the conditions of the absence of pertrurbations at $z \to -\infty$ and was expressed through A_1 and A_2.

The boundary conditions (7), (8) with an account of the set (10) and (11) read as

$$W'''(0) - (k_1^2 + 2k^2)W'(0) - k^3\omega_c^2 W(0)/(\omega\,\omega_\nu) = 0,$$
$$W''(0) + k^2 W(0) + \omega_T k^2 \Sigma_1(0)/\omega = 0, \quad (14)$$
$$T'(0) = 0,\ W'(-\infty) = W(-\infty) = T(-\infty) = 0;$$

$\omega_c^2 = (\sigma_0/\rho)k^3$, $\omega_T = (\sigma_T G_0)/(\nu\rho)$, $\omega_\nu = \nu k^2$, $\Sigma_1(0) = aW(0) + (\omega/G_0)T(0)$.

After the substitution (13) into (14) and the subsequent mathematical transformations, we obtain the set of equations as for A_1, A_2. The determinant of the set will be the dispersion equation. Represent this in terms of $R_\sigma - R_T = 0$, where

$$R_T = \omega_\nu \omega_T\{(1 - z_1/z_2)\delta(\omega^2 + 2\omega\omega_\nu + \omega_c^2) +$$
$$+ (1 - z_1/z_2)(2\omega\omega_\nu z_1 + \omega_c^2) + a\omega[\omega + 2\omega_\nu(1 - z_1)]\}, \quad (15)$$
$$R_\sigma = \omega^2[(\omega + 2\omega_\nu)^2 + \omega_c^2 - 4z_1\omega_\nu^2].$$

At $a = 0$, the dispersion equation ($R_\sigma - R_T = 0$) is [58]

$$\omega^2[(\omega + 2\omega_\nu)^2 + \omega_c^2 - 4z_1\omega_\nu^2] -$$
$$- \omega_\nu\omega_T[(1 - z_1/z_2)\delta(\omega^2 + 2\omega\omega_\nu + \omega_c^2) + (1 - 1/z_2)(2\omega\omega_\nu z_1 + \omega_c^2)] = 0 \quad (16)$$

If $a = 1$, $R_\sigma - R_T = 0$ results to (see [24]):

$$\omega^2[(\omega + 2\omega_\nu)^2 + \omega_c^2 - 4z_1\omega_\nu^2] -$$
$$- \omega_\nu\omega_T[(1 - z_1/z_2)\delta(\omega^2 + 2\omega\omega_\nu + \omega_c^2) + (1 - 1/z_2)(2\omega\omega_\nu z_1 + \omega_c^2)] =$$
$$= \omega[\omega + 2\omega_\nu(1 - z_1)]. \quad (17)$$

Using substitution $\omega = \omega_\nu(z_1^2 - 1)$ and the subsequent transformations, Eq. (17) can be reduced to the algebraic equation of the 16$^{\text{th}}$ power. In this case, the solutions satisfying the condition $\mathrm{Re}\,\omega > 0$, $\mathrm{Re}\,z_1 > 0$, and $\mathrm{Re}\,z_2 > 0$ will be unstable ones. The results of the numerical solution at the temperature gradient $G_0 = 2.9 \cdot 10^{10}$ K/m are depicted in Fig. 23. As follows from Fig. 23, the first two solutions of Eq. (17) are unstable ones.

There is an existence of two dependences of decrement on the wavelength. In the first case, the decrement maximum occurs at the wave-

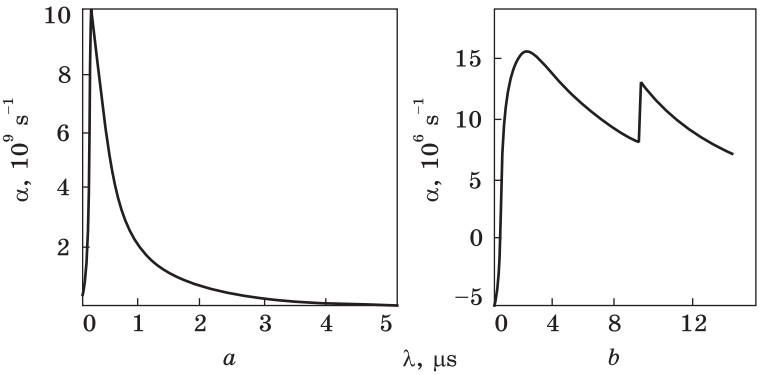

Fig. 23. Numerically calculated dependences of decrement on the wavelength (at $G_0 = 2.9 \cdot 10^{10}$ K/m) obtained solving Eq. (17), where both the first (*a*) and the second (*b*) roots of the equation are plotted

length $\lambda = 140$ nm, where $\alpha_{max} \approx 10^9$ s^{-1} (Fig. 23, *a*). The comparison with the experimental data of SEM showed that its values were 3–4 times less than the cells' dimensions. This disagreement can be attributed to the fact that the silicon effect on the value of surface tension, and its temperature dependence were not taken into account in the present research. The consideration of this effect will be in the scope of another paper. On the other hand, dependence α on λ (depicted in Fig. 23, *a*) is one-model one. Size distribution of high-speed crystallization cells has the same character. It permits to make a conclusion that thermocapillary instability explains adequately the one-modal character of the distribution. In the second case, two maximums occur at the wavelengths $\lambda = 2.6$ μm and $\lambda = 9.5$ μm (Fig. 23, *b*), where $\alpha_{max} \approx 10^6$ s^{-1}. When the temperature gradient value decreases, as in the first and second cases, the wavelengths, to which maximum of growth rate falls, increase. The presence of two decrement dependences on wavelength permits to suggest that the first dependence describes the initiation of crystallization cells on the surface, while the second one describes the formation of ordered (periodic) structures of its relief.

4. Summary and Conclusions

The modification of surface layer of hypoeutectic silumin АК10М2Н (87.88 wt.% of Al and 11.1 wt.% of Si as the base components diluted with minor impurities of Cu, Ni, Mg, Cr) by means of electron beam of various energy density (from 10 to 35 J/cm^2) was carried out. The complex of investigations of the physical and mechanical properties (microhardness, friction coefficient, wear resistance, *etc.*) of silumin after energy effect in various regimes for determination of their effective parameters was performed. As found, the microhardness value af-

ter EBT depends on the beam energy density and reaches the maximum values at the following treatment parameters: 25, 30, and 35 J/cm^2 (0.93 ± 0.052 GPa for 25 J/cm^2, 0.97 ± 0.71 GPa for 30 J/cm^2, 0.96 ± 0.103 GPa for 35 J/cm^2). Simultaneously, with an increase of microhardness in the irradiated samples, the decrease of friction coefficient and wear intensity was observed. In comparison with the material in as-received state, the friction coefficient decreased by ≈1.3 times, and the wear intensity decreased by ≈6.6 times. By the methods of atomic-force microscopy, we determined that the fine-gradient structure was formed in the treated layer, and the defects in the form of micropores were absent. The roughness of the treated layer of silumin samples ranges from 17 to 90 nm, while the roughness of the substrate near the treated layer varies in the range from 30 to 77 nm.

In the initial state, silumin is the multiphase aggregate, whose structure is presented by the grains of solid solution based on aluminium, the grains of eutectic Al–Si, the inclusions of the initial silicon, and intermetallides, whose dimensions and shape vary in wide limits. EBT results in the homogenization of silicon surface layers and the formation of multilayer gradient structure. The thickness of the homogenized layer varies depending on the parameters of electron-beam treatment and reaches the maximum values of 100 μm at energy density of 35 J/cm^2. At the density of electron-beam energy of 20 J/cm^2 along with more active dissolution of intermetallic phase, inclusions located in the surface layer of the material are observed. Due to the high surface-layer cooling rate, the elements forming the intermetallides make up the solid solution in the bulk of aluminium adjoining to the dissolving inclusion. The melting and high velocity cooling of silumin surface layer results in the formation of nanocrystalline structure of cellular crystallization, and the cells' dimensions vary within the range of 200–500 nm. The thickness of surface layer without the intermetallide particles varies within the range of 35–100 μm depending on the electron-beam energy density. The analysis of microelectron diffraction patterns shows that the cells of speed crystallization are formed by Al-based solid solutions. The interlayers' separation of the crystallization cells are the multiphase formations containing the particles of $Cu_{15}Si_4$, silicon as well as copper, and $A_{l4}Cu_9$. The intermetallide inclusions of cast origin located in the structure of cellular crystallization are revealed at the depth of 50–70 μm. They play the role of centres of cellular crystallization.

The elemental composition of silumin irradiated by electron beam varies in a regular way depending on the distance from the irradiation surface. The melting of silumin by intense pulsed electron beam is accompanied with the silicon concentration change in the surface layer up to 30 μm thick.

The EBT is accompanied with the graded structure formation: when moving away from the surface of treatment, the cellular crystallization structure transforms into the structure of mixed type, where the partially dissolved inclusions of cast origin are present along with the cells.

The formation mechanism of cellular and columnar crystallization structure consisting in the initiation of thermocapillary instability at vacuum molten metal interface is offered. Analysis of initial stage of thermocapillary instability development *via* the solving the dispersion equation for thermocapillary waves showed that the initiation of nanodimensional columnar structure according to this mechanism is adequately explained at the values of temperature gradient of $G_0 \sim 10^{10}$–10^{12} K/m. The solution of the complete dispersion equation shows that there exist two dependences of decrement on the wavelength. The first dependence has one maximum in nanodimensional range; it permits to conclude that it is responsible for the formation of cellular structure on the surface. The second dependence has two maximums in microdimensional range, which can be responsible for the formation of periodic structures on the material surface.

Acknowledgements. The authors express gratitude to K.A. Osintsev, V.V. Shlyarov, and K.A. Butakova for help in performing the experiments. The study was financially supported by state assignment of Ministry of Education and Science, RF (project No. 3.1283.2017/4.6).

REFERENCES

1. A.B. Belov, O.A. Bytsenko, A.V. Krainikov, A.F. Lvov, A.S. Novikov, A.G. Paikin, A.D. Teriaev, D.A. Teriaev, K.I. Tvagenko, V.A. Shulov, and V.I. Engelko, *Sil'notochnyye Impul'snyye Ehlektronnyye Puchki dlya Aviatsionnogo Dvigatelestroeniya* [High-Current Pulsed Electron Beams for Aircraft Engine Construction] (Moscow: Dipak: 2012) (in Russian).
2. V. Engelko, B. Yatsenko, G. Mueller, and Y. Bluhm, *Vacuum*, **62**: 211 (2001). https://doi.org/10.1016/S0042-207X(00)00446-2
3. G.E. Ozur, D.I. Proskurovsky, V.P. Rotshtein, and A.B. Markov, *Laser and Part. Beams*, **21**: 157 (2003). https://doi.org/10.1017/S0263034603212040
4. V.P. Rotshtein, Yu.F. Ivanov, D.I. Proskurovsky, K.V. Karlik, I.A. Shulepov, and A.B. Markov, *Surf. Coat. Tech.*, **180–181**: 382 (2004). https://doi.org/10.1016/j.surfcoat.2003.10.089
5. D.I. Proskurovsky, V.P. Rotshtein, G.E. Ozur, Yu.F. Ivanov, and A.B. Markov, *Surf. Coat. Tech.*, **125**: 49 (2000). https://doi.org/10.1016/S0257-8972(99)00604-0
6. P. Wenhai, H. Shengzhi, C. Jun, L. Wei, Z. Limin, D. Jun, *Int. J. Refr. Met. Hard Mat.*, **78**: 233 (2019). https://doi.org/10.1016/j.ijrmhm.2018.09.016
7. Y. Hangyu, C. Yuyong, W. Xiaopeng, and K. Fantao, *J. Alloys and Comp.*, **750**: 617 (2018). https://doi.org/10.1016/j.jallcom.2018.03.343
8. J. Wei, W. Langping, and W. Xiaofeng, *Nucl. Inst. Meth. Phys. Res. B*, **436**: 63 (2018). https://doi.org/10.1016/j.nimb.2018.09.003

9. P. Petrov, D. Dechev, N. Ivanov, T. Hikov, S. Valkov, M. Nikolova, E. Yankov, S. Parshorov, R. Bezdushnyi, and A. Andreeva, *Vacuum*, **154**: 264 (2018). https://doi.org/10.1016/j.vacuum.2018.05.026
10. B. Gao, N. Xu, and P. Xing, *Mat. Lett.*, **237**: 180 (2019). https://doi.org/10.1016/j.matlet.2018.11.054
11. Z. Chen, Y. Liu, H. Wu, W. Zhang, W. Guo, H. Tang, and N. Liu, *Appl. Surf. Sci.*, **357**: 2347 (2015). https://doi.org/10.1016/j.apsusc.2015.09.240
12. P. Yu, M. Yan, D. Tomus, C.A. Brice, C.J. Bettles, B. Muddle, and M. Qian, *Mat. Charact.*, **143**: 43 (2018). https://doi.org/10.1016/j.matchar.2017.09.005
13. B. Gao, S. Hao, J. Zou, W. Wu, G. Tu, and C. Dong, *Surf. Coat. Tech.*, **201**: 6297 (2007). https://doi.org/10.1016/j.surfcoat.2006.11.036
14. Y. Qin, C. Dong, X. Wang, S. Hao, A. Wu, J. Zou, and Y. Liu, *J. Vac. Sci. Tech. A*, **21**: 1934 (2003). https://doi.org/10.1116/1.1619417
15. J. Zou, Y. Qin, C. Dong, X. Wang, W. Almin, and S. Hao, *J. Vac. Sci. Tech. A*, **22**: 545 (2004). https://doi.org/10.1116/1.1697481
16. Yu.F. Ivanov, V.E. Gromov, S.V. Konovalov, D.V. Zagulyaev, E.A. Petrikova, and A.P. Semin, *Usp. Fiz. Met.*, **19**, No. 2: 195 (2018). https://doi.org/10.15407/ufm.19.02.195
17. D. Lu, B. Gao, G. Zhu, J. Lv, and L. Hu, *High Temp. Mat. Process.*, **36**: 97 (2017). https://doi.org/10.1515/htmp-2015-0092
18. B. Gao, L. Hu, S. Li, Y. Hao, Y. Zhang, and G. Tu, *Appl. Surf. Sci.*, **346**: 147 (2015). https://doi.org/10.1016/j.apsusc.2015.04.029
19. J. Feng, H. Wu, J. He, B. Zhang, *Mat. Charact.*, **54**: 99 (2005). https://doi.org/10.1016/j.matchar.2004.11.006
20. V.D. Sarychev, S.A. Nevskii, S.V. Konovalov, A.Yu. Granovskii, and V.E. Gromov, *Mat. Res. Express*, **6**: 026540 (2019). https://doi.org/10.1088/2053-1591/aaec1f
21. S. Biamino, A. Penna, U. Ackelid, S. Sabbadini, and O. Tassa, *Intermetallics*, **19**: 776 (2011). https://doi.org/10.1016/j.intermet.2010.11.017
22. D.V. Zagulyaev, S.V. Konovalov, V.E. Gromov, A.M. Glezer, Yu.F. Ivanov, and R.V. Sundeev, *Mat. Lett.*, **229**: 377 (2018). https://doi.org/10.1016/j.matlet.2018.07.064
23. F.Kh. Mirzoev, V.Ya. Panchenko, and L.A. Shelepin, *Phys.-Usp.*, **39**: 1 (1996). https://doi.org/10.1070/PU1996v039n01ABEH000125
24. E.B. Levchenko and A.L. Chernyakov, *Sov. Phys. JETP*, **54**: 102 (1981).
25. E.B. Levchenko and A.L. Chernyakov, *Fiz. Kh. Obr. Mat.*, **1**: 129 (1983) (in Russian).
26. M. Takashima, *J. Phys. Soc. Japan*, **50**: 2745 (1981). https://doi.org/10.1143/JPSJ.50.274
27. E.A. Ryabitskii, *Fluid Dynamics*, **27**: 313 (1992). https://doi.org/10.1007/BF01051176
28. M.G. Velarde, P.L. Garcia-Ybarra, and J.L. Castillo, *Phys. Chem. Hydr.*, **9**: 387 (1987).
29. I. Hashim and S.K. Wilson, *Z. angew. Math. Phys.*, **50**: 546 (1999). https://doi.org/10.1007/s000330050165
30. V.D. Sarychev, S.A. Nevskii, S.V. Konovalov, I.A. Komissarova, and E.V. Chermushkina, *IOP Conf. Ser. Mater. Sci. Eng.*, **91**: 012028 (2015). https://doi.org/10.1088/1757-899X/91/1/012028
31. S.V. Konovalov, X. Chen, V.D. Sarychev, S.A. Nevskii, V.E. Gromov, and M. Trtica, *Metals*, **7**: 1 (2017). https://doi.org/10.3390/met7010004
32. Yu.F. Ivanov, O.V. Krysina, M. Rygina, E.A. Petrikova, A.D. Teresov, V.V. Shugurov, O. V. Ivanova, and I. A. Ikonnikova, *High. Temp. Mat. Process.*, **18**, No. 4: 311 (2014). https://doi.org/10.1615/HighTempMatProc.2015015710

33. Yu.F. Ivanov and N.N. Koval, *Nizkoehnergeticheskie Ehlektronnyye Puchki Submillisekundnoy Dlitel'nosti Vozdeistviya: Poluchenie i Nekotoryye Aspekty Primeneniya v Oblasti Materialovedeniya* [Low-Energy Electron Beams of Submillisecond Exposure Duration: Production and Some Aspects of Application in Materials Science] (Ed. A. I. Potekaeva) (Tomsk: Publishing House of NTL: 2007) (in Russian).
34. K.V. Sosnin, V.E. Gromov, and Yu.F. Ivanov, *Struktura, Fazovyy Sostav i Svoistva Titana Posle Ehlektrovzryvnogo Legirovaniya Ittriem i Ehlektronno-Puchkovoy Obrabotki* [Structure, Phase Composition and Properties of Titanium after Electroexplosive Doping with Yttrium and Electron Beam Processing] (Novokuznetsk: Poligrafist: 2015) (in Russian).
35. C.A. Schuh, *Mater. Today*, **9**: 32 (2007). https://doi.org/10.1016/S1369-7021(06)71495-X
36. *Modul' Obrabotki Izobrazheniy Image Analysis P9: Spravochnoye Rukovodstvo* [Image Analysis P9: Reference Guide] (Zelenograd: NT-MDT: 2016) (in Russian).
37. *Sherokhovatost' Poverkhnosti. Terminy i Opredeleniya* [Surface Roughness. Terms and Definitions.]: GOST 25142-82 (1982) (in Russian).
38. *Transmission Electron Microscopy Characterization of Nanomaterials* (Ed. Challa S. S. R. Kumar) (Berlin–Heidelberg: Springer-Verlag: 2014). https://doi.org/10.1007/978-3-642-38934-4
39. *Transmission Electron Microscopy* (Eds. B. Carter and D. B. Williams) (Springer International Publishing Switzerland: 2016). https://doi.org/10.1007/978-3-319-26651-0
40. R.F. Egerton, *Physical Principles of Electron Microscopy: An Introduction to TEM, SEM, and AEM* (Springer International Publishing Switzerland: 2016). https://doi.org/10.1007/978-3-319-39877-8
41. A.G. Prigunova, N.A. Belov, and Yu.N. Taran, *Siluminy. Atlas Mikrostruktur i Fraktogramm Promyshlennykh Splavov* [Silumins. Atlas of Microstructures and Fractographs of Industrial Alloys] (Moscow: MISiS: 1996) (in Russian).
42. Yu.V. Milman, S.I. Chugunova, I.V. Goncharova, and A.A. Golubenko, *Usp. Fiz. Met.*, **19**, No. 3: 271 (2018). https://doi.org/10.15407/ufm.19.03.271
43. A.P. Laskovnev, Yu.F. Ivanov, amd E.A. Petrikova, *Modifikatsiya Struktury i Svoistv Ehvtekticheskogo Silumina Ehlektronno-Ionno-Plazmennoy Obrabotkoy* [Modification of the Structure and Properties of Eutectic Silumin by Electron–Ion–Plasma Treatment] (Minsk: Navuka: 2013) (in Russian).
44. S.V. Panin, A.E. Kolgachev, Yu.I. Pochivalov, V.E. Panin, and I.G. Goriacheva, *Fizicheskaya Mezomekhanika*, **8**: 101 (2005) (in Russian).
45. Yu. F. Ivanov and N. N. Koval, *Struktura i Svoistva Perspektivnykh Metallicheskikh Materialov* [Structure and Properties of the Promising Metallic Materials] (Ed. A. Potekaev) (Tomsk: Publishing House of NTL: 2007), Ch. 13, p. 345 (in Russian).
46. V. Rotshtein, Yu. Ivanov, and A. Markov, *Materials Surface Processing by Directed Energy Techniques* (Ed. Y. Pauleau) (Amsterdam: Elsevier Science: 2006), Ch. 6, p. 205.
47. Yu. A. Denisova, Yu.F. Ivanov, and O.V. Ivanova, *Ehvolyutsiya Struktury Poverkhnostnogo Sloya Stali, Podvergnutoy Ehlektronno-Ionno-Plazmennym Metodam Obrabotki* [Evolution of the Structure of the Steel Surface Layer Subjected to Electron–Ion–Plasma Processing Methods] (Eds. N.N. Koval and Yu.F. Ivanov) (Tomsk: Publishing House of NTL: 2007).
48. Yu. Ivanov, K. Alsaraeva, V. Gromov, S. Konovalov, and O. Semina, *Mat. Sci. Technol.*, **31**: 1523 (2015). https://doi.org/10.1179/1743284714Y.0000000727

49. N.A. Belov, S.V. Savchenko, and A.V. Hvan, *Fazovyy Sostav i Struktura Siluminov* [Phase Composition and Structure of Silumins] (Moscow: MISiS: 2008) (in Russian).
50. V.S. Zolotorevskiy and N.A. Belov, *Metallovedenie Liteinykh Alyuminievykh Splavov* [Metal Science of Cast Aluminium Alloys] (Moscow: MISiS: 2005) (in Russian).
51. N.A. Belov, *Fazovyy Sostav Alyuminievykh Splavov* [Phase Composition of Aluminium Alloys] (Moscow: MISiS: 2009) (in Russian).
52. G.B. Stroganov, V.A. Rotenberg, and G.B. Gershman, *Splavy Alyuminiya s Kremniem* [Aluminium Alloys with Silicon] (Moscow: Metallurgiya: 1977) (in Russian).
53. A.P. Babichev, *Fizicheskie Velichiny: Spravochnik* [Physical Quantities: Handbook] (Eds. I.S. Grigorieva and E.Z. Meilikhov) (Moscow: Energoatomizdat: 1991) (in Russian).
54. D. Brandon and U. Kaplan, *Mikrostruktura Materialov. Metody Issledovaniya i Kontrolya* [Microstructure of Materials. Methods of Study and Control] (Moscow: Tekhnosfera: 2006) (in Russian).
55. B. Cheynet, J.-D. Dubois, and M. Milesi, *Technique de l'Ingenier, Traité Materiaux Metalliques* (Strasbourg: Imprimerie Strasbourgeoise: 1993), p. M 64-1 (in French).
56. A. Samarskii, P.N. Vabishchevich, O.P. Iliev, and A.G. Churbanov, *Int. J. Heat Mass Transfer.*, **36**: 4095 (1993). https://doi.org/10.1016/0017-9310-(93)90071-D
57. Y.F. Ivanov, E.A. Petrikova, O.V. Ivanova, I.A. Ikonnikova, and A.V. Tkachenko, *Rus. Phys. J.*, **58**: 478 (2015). https://doi.org/10.1007/s11182-015-0524-7
58. E. Aursand, S.H. Davis, and T. Ytrehus, *J. Fluid Mech.*, **852**: 283 (2018). https://doi.org/10.1017/jfm.2018.545
59. V.A. Urpin and D.G. Yakovlev, *Zh. Tekhn. Fiz.*, **59**, No. 2: 19 (1989) (in Russian).

Received March 26, 2019;
in final version, August 17, 2019

Ю.Ф. Іванов[1,2], *Д.В. Загуляєв*[3], *С.А. Невський*[3],
В.Є. Громов[3], *В.Д. Саричев*[3], *А.П. Семін*[3]

[1] Інститут сильнострумової електроніки СВ РАН,
просп. Академічний, 2/3, 634055 Томськ, Росія
[2] Національний дослідницький Томський політехнічний університет,
просп. Академічний, 2/3, 634055 Томськ, Росія
[3] Сибірський державний індустріальний університет,
вул. Кірова, 42, 654007 Новокузнецьк, Росія

МІКРОСТРУКТУРА ТА ВЛАСТИВОСТІ ДОЕВТЕКТИЧНОГО СИЛУМІНУ, ОБРОБЛЕНОГО ПОТУЖНЬОСТРУМОВИМИ ІМПУЛЬСНИМИ ЕЛЕКТРОННИМИ ПУЧКАМИ

Методами сучасного фізичного матеріалознавства досліджено структурно-фазові стани, мікротвердість і трибологічні властивості доевтектичного силуміну після електронно-пучкового оброблення. Об'єктом дослідження був доевтектичний силумін марки АК10М2Н із вмістом 87,88 ваг.% Al й 11,1 ваг.% Si як головних компонентів. Поверхню силуміну піддавали електронно-пучковому обробленню в шістьох різних режимах, що різняться густиною енергії пучка електронів. Міряння мікротвердости модифікованих поверхневих шарів силуміну уможливили

визначення трьох оптимальних режимів впливу (з густинами енергії пучка електронів у 25, 30 і 35 Дж/см^2), за яких мікротвердість підданих модифікації шарів перевищує мікротвердість литого силуміну: 0,86 ± 0,041 ГПа — литий стан; 0,93 ± 0,052 ГПа — для 25 Дж/см2; 0,97 ± 0,071 ГПа — для 30 Дж/см^2; 0,96 ± 0,103 ГПа — для 35 Дж/см^2. Виявлено, що електронно-пучкове оброблення з оптимальними параметрами призводить до формування поверхні, механічні та трибологічні характеристики якої значно перевищують відповідні значення для силуміну литого стану. Дані атомно-силової мікроскопії корелюють з результатами стосовно мікротвердости. Оброблені за представленими режимам зразки характеризуються дрібнозернистою комірчастою структурою, а також мають найменшу шерсткість обробленого шару (17–33 нм) і підкладинки (45–57 нм) порівняно з іншими режимами. Встановлено, що в обробленому шарі формується дрібнозерниста, ґрадієнтна, комірчаста структура, яка в міру віддалення від поверхні оброблення перетворюється у структуру змішаного типу. Товщина гомогенізованого шару варію залежно від параметрів електронно-пучкового оброблення і сягає максимальних значень у 100 мкм при густині енергії у 35 Дж/см^2. Виявлено, що модифікований шар вільний від інтерметалідів і складається із нанокристалічної структури комірчастої кристалізації. Висловлено припущення, що ці два чинники спричинюють підвищення механічних і трибологічних характеристик модифікованого шару. Запропоновано механізм утворення структури комірчастої та стовпчастої кристалізації, який полягає у виникненні термокапілярної нестійкости на межі поділу «випарувана речовина/рідка фаза». Розроблено математичний модель теплового впливу електронного пучка на поверхневі шари силуміну.

Ключові слова: фізична природа, математичні моделі, структура, властивості, доевтектичний силумін, електронно-променеве оброблення, фазовий склад.

Ю.Ф. Иванов[1,2], *Д.В. Загуляев*[3], *С.А. Невский*[3], *В.Е. Громов*[3], *В.Д. Сарычев*[3], *А.П. Семин*[3]

[1] Институт сильноточной электроники СО РАН, просп. Академический, 2/3, 634055 Томск, Россия

[2] Национальный исследовательский Томский политехнический университет, просп. Академический, 2/3, 634055 Томск, Россия

[2] Сибирский государственный индустриальный университет, ул. Кирова, 42, 654007 Новокузнецк, Россия

МИКРОСТРУКТУРА И СВОЙСТВА ДОЭВТЕКТИЧЕСКОГО СИЛУМИНА, ОБРАБОТАННОГО СИЛЬНОТОЧНЫМИ ИМПУЛЬСНЫМИ ЭЛЕКТРОННЫМИ ПУЧКАМИ

Методами современного физического материаловедения исследованы структурно-фазовые состояния, микротвёрдость и трибологические свойства доэвтектического силумина после электронно-пучковой обработки. Объектом исследования являлся доэвтектический силумин марки АК10М2Н с содержанием 87,88 вес.% Al и 11,1 вес.% Si как главных компонентов. Поверхность силумина подвергалась электронно-пучковой обработке в шести различных режимах, отличающихся плотностью энергии пучка электронов. Измерения микротвёрдости модифицированных поверхностных слоёв силумина позволили определить три оптимальных режима воздействия (с плотностями энергии пучка электронов 25, 30 и 35 Дж/см^2), при которых микротвёрдость повергнутых модификации слоёв превышает микротвёрдость литого силумина: 0,86 ± 0,041 ГПа — литое состояние; 0,93 ± ± 0,052 ГПа — для 25 Дж/см^2; 0,97 ± 0,071 ГПа — для 30 Дж/см^2; 0,96 ±

± 0,103 ГПа — для 35 Дж/см^2. Обнаружено, что электронно-пучковая обработка с оптимальными параметрами приводит к формированию поверхности, механические и трибологические характеристики которой значительно превышают соответствующие значения для силумина литого состояния. Данные атомно-силовой микроскопии коррелируют с результатами по мик-ротвёрдости. Обработанные по представленным режимам образцы ха-рактеризуются мелкозернистой ячеистой структурой, а также имеют наименьшую шероховатость обработанного слоя (17–33 нм) и подложки (45–57 нм) по сравнению с другими режимами. Установлено, что в обработанном слое формируется мелкозернистая, градиентная, ячеистая структура, которая по мере удаления от поверхности обработки превращается в структуру смешанного типа. Толщина гомогенизированного слоя варьируется в зависимости от параметров электронно-пучковой обработки и достигает максимальных значений 100 мкм при плотности энергии 35 Дж/см^2. Обнаружено, что модифицированный слой свободен от интерметаллидов и состоит из нанокристаллической структуры ячеистой кристаллизации. Высказано предположение, что эти два фактора являются причиной повышенных механических и трибологических характеристик модифицированного слоя. Предложен механизм образования структуры ячеистой и столбчатой кристаллизации, который заключается в возникновении термокапиллярной неустойчивости на границе раздела «испарённое вещество/жидкая фаза». Разработана математическая модель теплового воздействия электронного пучка на поверхностные слои силумина.

Ключевые слова: физическая природа, математические модели, структура, свойства, доэвтектический силумин, электронно-пучковая обработка, фазовый состав.